Master of Science

One-pot hydrothermal of Interface-Functionalized of Hematite Nanocrystals for Enhanced Oxygen Evolution Reaction

The Graduate School of the University of Ulsan

School of Chemical Engineering

Thai Thi Dac Ngan

One-pot hydrothermal of Interface-Functionalized of Hematite Nanocrystals for Enhanced Oxygen Evolution Reaction

Supervisor: Professor Seung Hyun Hur

A Dissertation

Submitted to
the Graduate School of the University of Ulsan
In partial Fulfillment of the Requirements
for the Degree of

Master

by

Thai Thi Dac Ngan

School of Chemical Engineering
University of Ulsan, Korea
August 20

One-pot Hydrothermal Synthesis of Interface-Functionalized Hematite Nanocrystals for Enhanced Oxygen Evolution Reaction

This certifies that the master's thesis of Thai Thi Dac Ngan is approved.

Won Mook Choi

Committee Chair of Professor Chair Won Mook Choi

Seung Hyun Hur

Committee Member of Professor Seung Hyun Hur

Committee Member of Professor Sung Gu Kang

School of Chemical Engineering

University of Ulsan, Korea

August 2024

Acknowledgement

First and foremost, I would like to express my sincere gratitude to my supervisor, Professor Seung Hyun Hur, for Professor's continuous support, guidance, and invaluable insights throughout the research and writing process. Professor's expertise, patience, and encouragement have been instrumental in the successful completion of this thesis.

I would also like to extend my heartfelt appreciation to the members of my thesis committee, Professor Won Mook Choi and Professor Sung Gu Kang, for their insightful feedback, constructive criticism, and thought-provoking discussions, which have greatly contributed to the quality and depth of this work.

I am deeply grateful to the faculty and staff of the School of Chemical Engineering at University of Ulsan for their support and for providing me with the necessary resources and opportunities to pursue my research interests. Special thanks go to my dearest lab members – my senior Dr. Tran Van Phuc along with Dr. Jayasmita Jannah, Dr. Le Van Nam, Dr. Aniruddha, Huynh Ngoc Diem, Tran Duc Viet for their assistance, valuable advice, and beloved encouragement during various stages of this project. Besides, thanks to my bestie Huynh Ngoc Khanh and Pham Ngoc Nhiem, I had many enjoyable times in Korea.

Finally, I would like to express my heartfelt appreciation to my family and friends for their unwavering support, encouragement, and understanding throughout my graduate studies. Their love and belief in me have been a constant source of motivation and inspiration. Despite homesickness and hurdles, their encouragement has been the steady hand that propelled me forward.

Abstract

This report presents a novel methodology for the surface fabrication of electrocatalysts, where hematite is interface-functionalized using organic ligands to enhance the oxygen evolution reaction (OER) performance. All the synthesized samples exhibit a nanoparticle morphology and a crystalline structure consistent with hematite, which is the most stable iron oxide. The functional groups from benzimidazole (bIm) and/or caffeine (Caf) serve as scaffolds and sources of carbon, hydrogen, oxygen, and nitrogen, facilitating metal-support interactions (MSIs) to enhance OER activity. The optimal catalyst, Fe-(bIm)0.3Caf, is synthesized by a combination of predominantly bIm with 30% Caf substitution, which introduces defects and oxygen vacancies, resulting in superior OER performance compared to single-ligand counterparts. The Fe-(bIm)0.3Caf catalyst exhibits the lowest overpotential of 264 mV at 10 mA cm−2 and the smallest Tafel slope of 30 mV dec^{-1}, outperforming commercial Fe_2O_3. This highlights the importance of the surface engineering strategy, which modifies the surface and electronic structure of metal nanostructures to achieve efficient OER activity. The report outlines a one-pot hydrothermal process for preparing interface-functionalized hematite nanocrystals at low temperatures, offering a promising approach for achieving efficient and durable OER electrocatalysts.

Keywords Oxygen evolution reaction, oxygen vacancies, nanoparticle, one-pot hydrothermal, surface engineering, interface-functionalized

Contents

List of Figure

List of Table

1. Background

1.1 Overview

The world is facing major challenges related to escalating energy demand, energy crises, environmental pollution, and abnormal climate change. Annual global emissions of carbon dioxide 1940-2023 (**Figure 1**). Global carbon dioxide (CO_2) emissions from fossil fuels and industry reached 37.15 billion metric tons ($GtCO_2$) in 2022. Emissions are projected to rise 1.1% in 2023, reaching a record high of 37.55 $GtCO_2$. Since 1990, global CO_2 emissions have increased by over 60% .[1] These emissions are primarily driven using coal, oil, and natural gas for combustion, industrial processes, gas flaring, and cement manufacturing. The continuous growth in CO_2 emissions is a significant concern, reflecting the world's reliance on fossil fuels despite the need to transition towards more sustainable energy sources. Energy supply is a critical issue for the sustainable development of modern society, especially in the face of continued population growth, depletion of fossil fuel resources, and the worsening effects of climate change.

In response to these challenges, there have been tremendous research efforts, both in academic and industrial communities, to develop advanced techniques for harvesting renewable energy sources, including biofuels, wind, solar, geothermal, and hydroelectric power. The transition to a more sustainable energy future is paramount for the long-term well-being of our planet and its inhabitants. Water splitting is a promising solution for harvesting renewable energy sources and addressing the global energy and environmental challenges (**Figure 2**).[2]

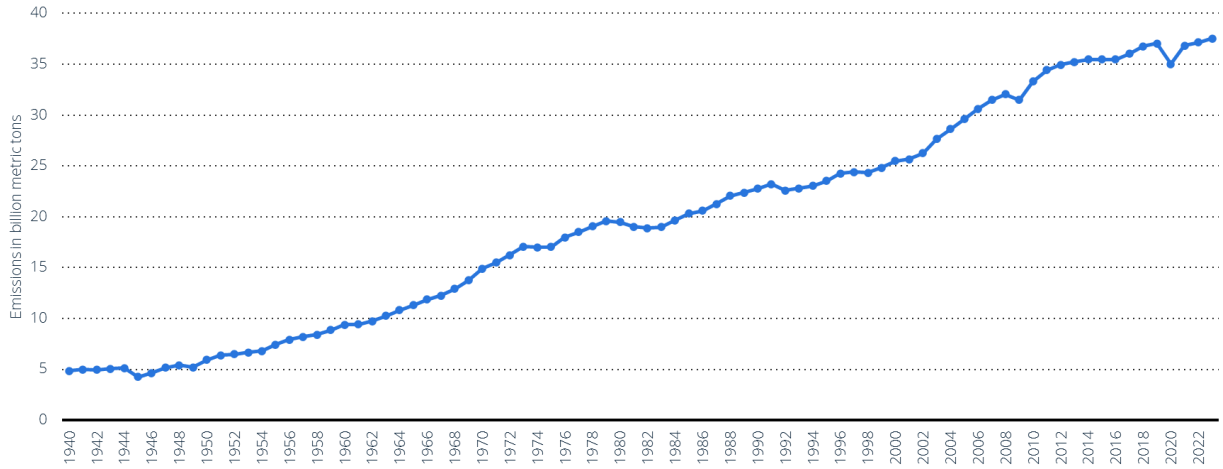

Figure 1. Annual carbon dioxide (CO_2) emissions worldwide from 1940 to 2023 (in billion metric tons).[1]

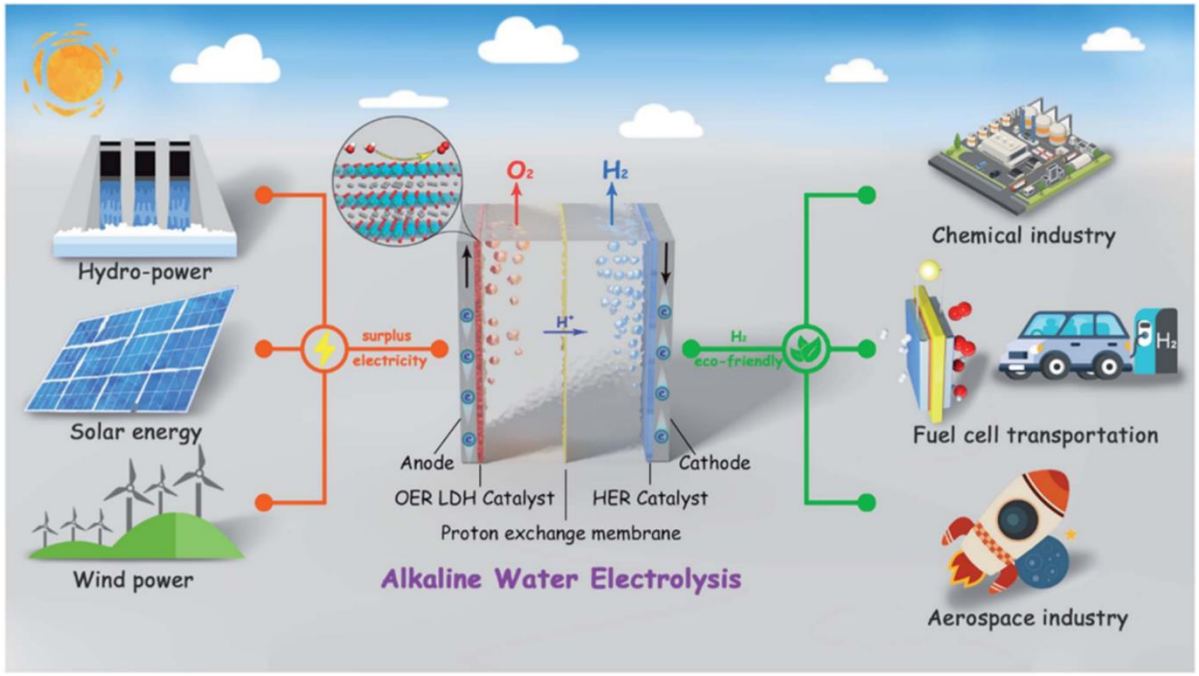

Figure 2. A sustainable energy system based on an integrated water electrolysis system for renewable hydrogen fuel generation.[2]

Water splitting, also known as water electrolysis, is a fundamental process in the field of renewable energy and hydrogen production. It involves the decomposition of water into its constituent elements H_2 and O_2, through the application of an external energy source. Water splitting is driven by an electrochemical reaction that takes place in an electrolyzer, a device that uses electricity to split water molecules. In a typical water electrolysis system, water is fed into the electrolyzer, where it undergoes a series of reactions at the anode and cathode electrodes (**Figure 3**).[3-5]

At the anode, water molecules are oxidized, releasing electrons, and producing oxygen gas:

$2H_2O \rightarrow O_2 + 4H+ + 4e^-$

At the cathode, the released electrons reduce hydrogen ions (protons) to form hydrogen gas:

$4H+ + 4e^- \rightarrow 2H_2$

The overall reaction can be represented as: $2H_2O \rightarrow 2H_2 + O_2$

This process is highly efficient and can be powered by renewable energy sources, such as solar, wind, or hydropower, making it a promising approach to produce clean, sustainable hydrogen fuel. Hydrogen produced through water splitting can be used in a variety of applications, including fuel cells for transportation, stationary power generation, and industrial processes.[2] Additionally, the oxygen byproduct can be utilized in various industries, further enhancing the overall efficiency and sustainability of the water splitting process.

Water splitting has been the subject of extensive research and development, with ongoing efforts to improve the efficiency, cost-effectiveness, and scalability of the technology. As the global demand for clean energy and sustainable fuel sources continues to grow, water splitting is poised to play a crucial role in the transition towards a more environmentally-friendly energy future.

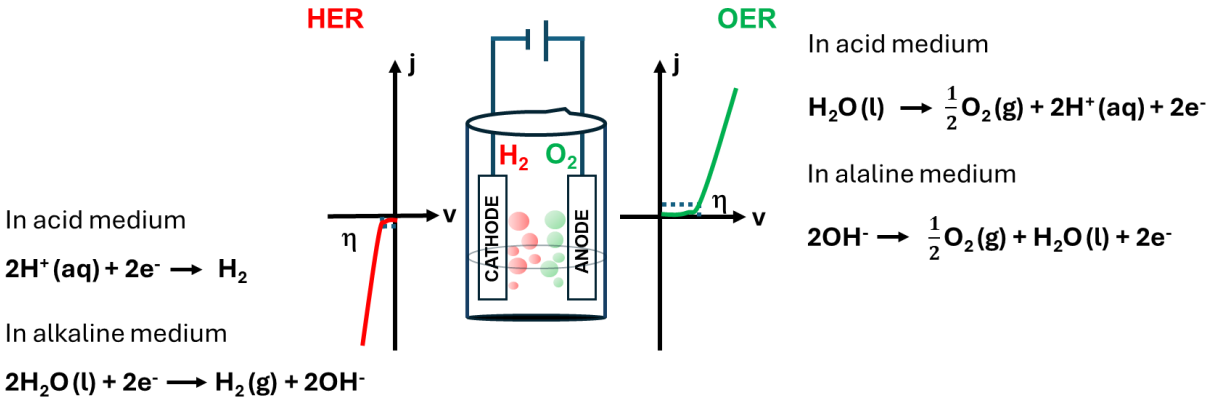

Figure 3. Overall water splitting

1.2 Oxygen evolution reaction

Oxygen evolution reaction (OER) is one of the primary mechanisms that regulate the efficiency of water electrolysis. The use of appropriate catalysts is essential to minimize the energy wastage during OER mechanism and enhance the OER efficiency. Currently, IrO_2 and RuO_2 are considered the most active OER catalysts.[6] However, the high cost and scarcity of these materials hinder their widespread applications.[7] Considering the significance of water electrolysis in sustainable fuel production, the fabrication of low-cost and highly effective catalysts is imperative, particularly for large-scale applications.

OER is a complex electrochemical reaction involving four electron–proton transfer processes and multiple reaction intermediates. The OER mechanism generally comprises the adsorbate evolution mechanism (AEM) and lattice oxygen-mediated mechanism (LOM) (**Figure 4**). In the AEM, H_2O initially absorbs onto the active site (M) through a one-electron oxidation process, forming M−*OH species. The subsequent proton coupling and electron removal from M−*OH produce M−*O species. Thereafter, the M−*O species reacts with H_2O to form M−*OOH, releasing O_2 via a one-electron oxidation reaction. In contrast to the AEM, in the LOM, the formed M−*O species couples with lattice oxygen, releasing O_2 and forming oxygen vacancies.[8] Previous reports suggest that LOM-based catalysts offer significantly improved OER activity compared to AEM. However, during OER, issues related to catalyst reconstruction and instability frequently arise. Therefore, achieving a balance between the AEM and LOM is essential for realizing optimal activity and stability for OER.[9]

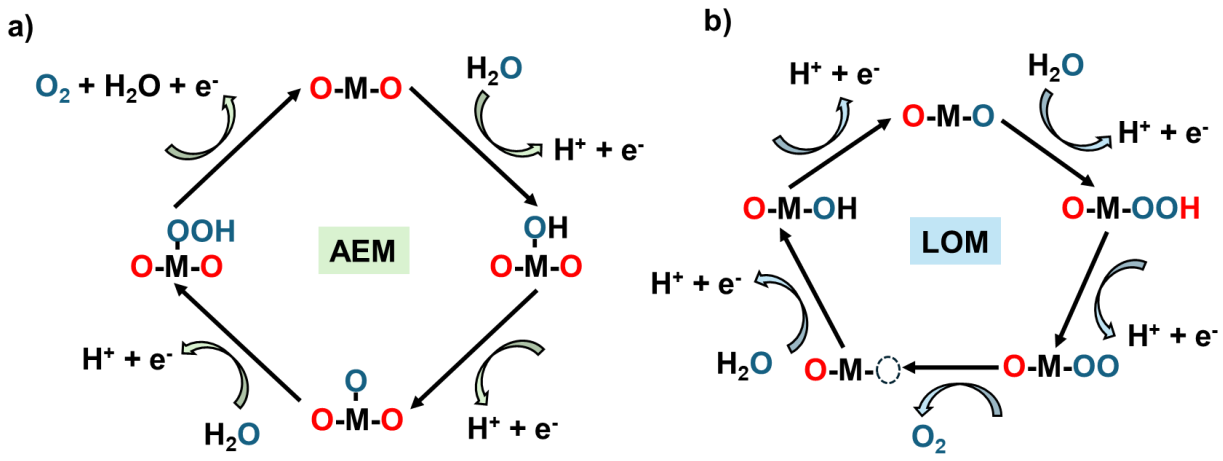

Figure 4. OER mechanism involving a) AEM and b) LOM

2. Fundamental parameters for evaluating electrochemical reaction

2.1 Overpotential

To facilitate electrocatalytic water splitting, the applied potential needs to surpass the equilibrium potential to overcome the electrode kinetic barrier of the reaction. This difference between the applied potential required to drive a reaction and the potential of the reaction under equilibrium conditions is termed as overpotential (η), as illustrated in following equation:

$$\eta = E - E_{eq}$$

Overpotential stands as a pivotal metric for assessing electrocatalyst performance. Thus, reducing overpotential emerges as a paramount objective in electrocatalyst design, fostering enhanced efficiency in energy conversion systems. A lower overpotential signifies superior electrocatalytic prowess for the intended reaction. This parameter is typically determined through linear scan voltammetry (LSV) curves, employing iR correction to compensate for electrolyzer resistance. It represents the additional potential required to attain a designated current density, often benchmarked at 10 mA cm^{-2} to evaluate and compare electrocatalyst activity.[10]

2.2 Tafel slope and exchange current density

The Tafel slope is a measure of the reaction kinetics in electrochemical processes, represented by a linear plot of overpotential (η) versus the logarithm of current density (log i). A lower Tafel slope indicates a faster and more reversible reaction. The Tafel equation can be applied to both HER and OER in the water splitting process. Understanding the Tafel slope is crucial for optimizing the performance of water splitting systems. The Tafel slope can be determined experimentally through LSV measurements, providing valuable insights into the reaction kinetics and guiding the development of improved catalysts and system designs for water splitting applications.[4]

$$\eta = a + b\log(i)$$

η : overpotential

a: intercept relative to the exchange current density

b: Tafel slope (mV dec^{-1})

i: current density (mA^{-2})

In summary, the Tafel slope is a key parameter for evaluating the efficiency and reversibility of electrochemical reactions, particularly in the context of water splitting, and its practical determination is an important tool for optimizing the performance of these technologies.

2.3 Stability

For practical applications, the stability of electrocatalysts is a crucial parameter to evaluate. Catalyst stability is typically measured by recording the change in current over time at a fixed potential or current, using techniques such as chronopotentiometry or chronoamperometry. To comprehensively assess the durability of catalysts, a multicurrent step chronopotentiometry technique can be employed. This involves measuring the potential response over a wide range of current densities, from 10 mA cm^{-2} to hundreds or even thousands of mA cm^{-2} Another impactful method for evaluating catalyst stability is to compare the LSV curves before and after the electrochemical reaction. Any evident decay in the performance of the catalyst can be easily detected through this approach. The stability and durability of electrocatalysts are critical factors for their practical application in energy conversion and storage devices. Thorough evaluation of these parameters, using techniques like chronopotentiometry, chronoamperometry, and LSV comparisons, provides valuable insights into the long-term performance and reliability of the catalysts.

2.4 Electrochemical active Surface Area

Specific activity assesses the catalyst's activity relative to its electrochemical active surface area (ECSA). ECSA provides valuable insight into the active sites of the material, which are crucial for electrocatalysis. The number of active sites directly influences the catalyst's ability to adsorb water molecules and intermediates efficiently. Therefore, a larger ECSA is advantageous for electrocatalysts involved in water

splitting processes. In essence, both mass activity and specific activity metrics play significant roles in characterizing the effectiveness of electrocatalysts for water splitting applications.[11-13]

2.5 Electrochemical Impedance Spectroscopy

Electrochemical Impedance Spectroscopy (EIS) measurements provide valuable insights into charge transfer resistances (Rct), which directly impact electrode kinetics. High charge transfer resistances indicate obstacles to electron transfer, resulting in slower reaction rates for the electrocatalyst. Therefore, electrocatalysts with lower charge transfer resistances are more conducive to efficient electron transfer, facilitating faster reaction kinetics.

3. Interface-Functionalized Hematite Nanocrystals for Oxygen Evolution Reaction

3.1 Introduction

Interface functionalization can modify the chemistry of the electrode material's surface to impart specific properties relevant to the intended applications. Various functionalization methods reported in the literature can alter the surface energy of the materials. This modification can facilitate better coupling with other targeted substances at the molecular level. Nowadays, the functionalization process has become an essential step in the preparation of efficient electrode materials. This section focuses on electrode materials designed for OER applications, particularly those related to functionalization with single ligand and dual ligands and doping with metal oxides and carbon skeletons. The functionalization of the electrode surface can tailor the material's properties to enhance its performance for the desired OER applications. This surface modification approach is widely employed to develop advanced electrode materials with improved characteristics.

Metal-support interactions (MSI) describe how the interplay between metals and their compounds influences the catalytic reaction process, particularly OER mechanisms. MSI explores the relationships between key performance indicators like activity, selectivity, and stability, as well as the intrinsic structures of catalysts, including their electronic and geometric properties. Strong interactions, such as electronic interactions, chemical bonding, and functional groups, can stabilize metal active centers on supports through chemical bonding and physical adsorption. MSI can alter the covalent states of metal active centers by facilitating charge transfer and electron redistribution, thereby improving the intrinsic activity for OER. Furthermore, MSI can modulate the adsorption energy of O-intermediates and change the reaction pathway of OER. Manipulating the MSI between metals and supports provides valuable guidelines for the rational design of efficient electrocatalysts.

Previous reports suggest that Fe_2O_3 is a crucial component of composite electrocatalysts that contributes to achieve high oxygen production ability. The beneficial properties of Fe_2O_3, such as abundance in the Earth's crust, ease of construction, environmental friendliness, high stability, and controllable shape, render it a valuable catalyst for fundamental and practical applications.[14, 15] However, challenges, such as the

sluggish reaction mechanism, which requires the removal of four electrons to form O_2, low electrical conductivity, and limited active sites, render the use of single oxides as electrocatalysts difficult.[16] Therefore, the interface functionalization of Fe_2O_3 with organic ligands, which can modify the surface and impact the electronic structure of metal nanostructures, is necessary. Organic ligands possess unique physical and chemical properties and can form metal nanostructures exhibiting exceptional catalytic selectivity toward certain reaction precursors.[17]

Additionally, the sample comprising mixed organic ligands (benzimidazole (bIm) and caffeine (Caf)), Fe-(bIm)0.3Caf, demonstrated a superior performance compared to other synthesized samples, Fe-bIm and Fe-Caf . This superiority can be attributed to the presence of oxygen vacancies, which are among the most common defects in metal oxides (MOs), and considerably increase the OER activity. The presence of oxygen vacancies in Fe-(bIm)0.3Caf enhances the electrocatalytic efficiency for OER by influencing the intermediate adsorption on the catalyst surface, modifying the electronic structure, and improving conductivity.[18]

Organic ligands act as carbon-supported catalysts with metal–support interactions (MSIs), which can alter the OER mechanism through electronic and geometric structural changes.[19] The covalent state of the metal–oxygen (M–O) bond significantly influences the reaction mechanism. As the covalence of the M−O bond increases, the reaction mechanism shifts from the AEM to the LOM.[20] This explains the superior OER activity of the interface-functionalized mixed-ligand Fe-(bIm)0.3Caf compared with that of commercial Fe_2O_3, which exhibits a significantly smaller overpotential. The MSIs stabilize metal compounds and enhance the covalence of the M–O bond, ensuring a balance between the AEM and LOM[19] and endowing Fe-(bIm)0.3Caf with higher durability than commercial Fe_2O_3. Furthermore, interface-functionalized hematite comprising α-Fe_2O_3 and functional groups, such as $–NH_2$ and –COOH, which play a crucial role in interface functionalization, exhibits a significantly enhanced OER catalytic performance compared to commercial Fe_2O_3.[21, 22] This is clearly observed in the case of the optimal

sample in this study, Fe-(bIm)0.3Caf, which exhibited distinct advantages over commercial Fe_2O_3 in terms of efficiency and durability. These results emphasize the effectiveness of interface engineering with the aforementioned functional groups in enhancing the OER activity.

Additionally, drawbacks of MOs as electrocatalyst, such as slow reaction kinetics, can be addressed by constructing electrodes with nanostructured morphologies.[23] Furthermore, α-Fe_2O_3 (hematite) demonstrates higher thermodynamic stability than the other iron oxides (IOs), such as magnetic nanoparticles, including magnetite, maghemite, and goethite,[24] in the presence of oxygen.[25] Among IOs, hematite is the optimal material for fabricating potential electrocatalysts with high durability.

Herein, we employed a one-pot hydrothermal approach to engineer interface-functionalized hematite nanocrystals to enhance the OER activity. Among the analyzed samples, the mixed-ligand sample, Fe-(bIm)0.3Caf, exhibited the highest performance, displaying the lowest overpotential of 260 mV at 10 mA cm^{-2} and the smallest Tafel slope of 30 mV dec^{-1}, which demonstrate the role of oxygen vacancies in determining the OER activity. Furthermore, Fe-(bIm)0.3Caf exhibiting long-term durability with high retention activity (99.57%) was compared with commercial Fe_2O_3 via a 30 h stability test, illustrating the importance of the interface-functionalization strategy. Additionally, surface functionalization can lead to the introduction of heteroatoms, including oxygen and nitrogen, in the carbon skeleton, modifying the electronic structure and adsorption energy of reaction intermediates. The dual roles, stemming from the oxygen vacancies and strength of MSIs originating from functional groups and heteroatoms in the carbon skeleton, enhance the conductivity, number of active sites, and catalytic activity of the prepared product, ultimately contributing to improve the OER activity. Therefore, this study provides a novel approach for engineering interface-functionalized hematite nanocrystals, focusing on improving the mixed ligands for enhancing the OER in alkaline media.

3.2 Experiment details

Chemicals

Iron (III) nitrate nonahydrate ($Fe(NO_3)_3.9H_2O$, 99.95%), benzimidazole (bIm, 98%) and commercial Iridium (IV) oxide IrO_2 were purchased from Sigma-Aldrich. Caffeine (Caf) was purchased from Daejung. N,N-dimethyl formamide (DMF), deioned water (H_2O), ethanol (95.5%), Solvents were obtained from commercial sources without further purification.

Characterization techniques

Field emission scanning electron microscopy (FE-SEM), High-Resolution Transmission Electron Microscopy (HR-TEM), Energy dispersive X-ray spectroscopy (EDS), X-ray diffraction (XRD), Fourier transform infrared (FT-IR) spectroscopy, Brunauer-Emmett-Teller (BET) analyzer, Thermogravimetric analysis (TGA), Electron paramagnetic resonance (EPR), X-ray photoelectron spectroscopy (XPS) were used to investigate the morphologies, atomic and molecule structure, functional groups linkage, surface area, oxygen vacancy and elemental compositions of the obtained products.

Preparation of interface-functionalized hematite nanocrystals

Interface-functionalized hematite nanocrystals preparation under facilitation of bIm and Caf ligands was illustrated in **Figure 5.** Caf and bIm were uniformly dispersed in a 20 ml DMF:H_2O mixture (5:5) and subsequently poured into another solution containing 1 mmol of $Fe(NO_3)_3.9H_2O$ in 20 ml of the solvent mixture under vigorous stirring for 30 min. A mixed-ligand sample, denoted as Fe-(bIm)0.3Caf, was prepared using 0.75 mmol of bIm and 0.25 mmol of Caf. Fe-bIm and Fe-Caf were synthesized using a similar methodology by adding only one type of ligand. The as-obtained uniform mixture was subsequently transferred to a stainless-steel autoclave and reacted at 100°C for 12 h. As-prepared material was cleansed via centrifugation and dried overnight at 60°C to obtain the final product.

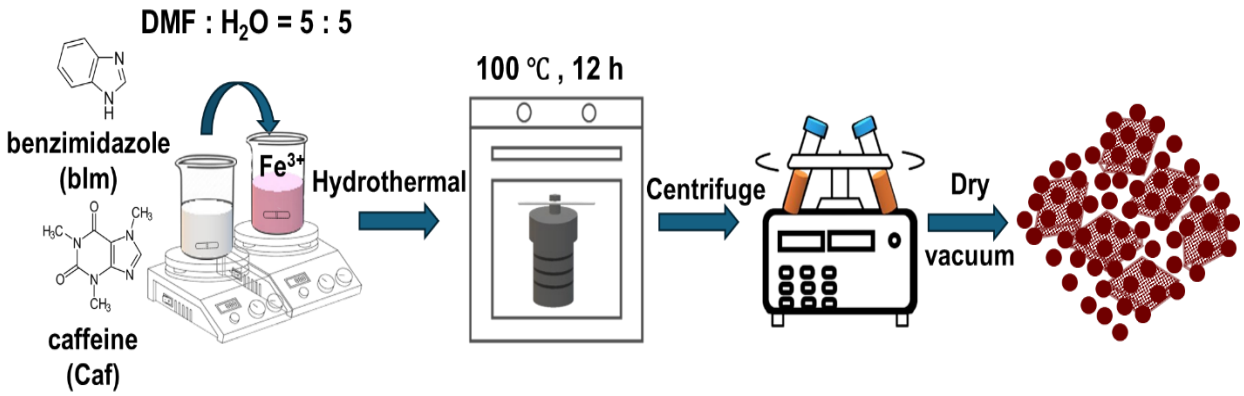

Figure 5. Schematic of the one-pot hydrothermal synthesis of interface-functionalized hematite

Electrochemical characterization

All electrochemical samples were analyzed using a standard three-electrode system that was powered by a VMP3 electrochemical workstation and used nickel foam (NF) as the working electrode in 1 M KOH that was saturated with nitrogen at room temperature. Graphite rod and Hg/HgO electrodes served as the counter and reference electrodes, respectively. After tests, electric potentials obtained were converted to reversible hydrogen electrode (RHE) following to the Nernst equation:

$$E_{RHE} = E_{Hg/HgO} + 0.094\ V + 0.059*pH$$

Overpotential (η) parameter was acquired following OER formula:

$$\eta = E_{RHE} - 1.23\ V$$

Prior to the preparation of the catalytic electrode, the nickel foams (NF) were cleaned by supporter device ultrasonicate in 1 M HCl, acetone, water and ethanol, respectively, and then dried vacuum at 60 ℃ for 24 h. Catalyst samples were dispersed 5 mg of every catalyst product into 980 μl of ethanol and water (ethanol : water = 5 : 5) and 20 μl of 0.5 wt % nafion by 30-min ultrasonication to prepare ink for deposition onto the bare NF. After collecting several of uniformed solutions, 400 μl was pipetted onto both sides of cleansed NF (1 cm X 1 cm) then followed by drying to get a series of catalytic electrodes.

Electrochemical measurement

The OER performance of all the samples was assessed in oxygen-saturated 1 M KOH for a duration of 10 min. To ensure an accurate electrochemical performance, the nickel foam catalyst-loaded electrodes were subjected to an initial conditioning process, involving consecutive cyclic voltammetry (CV) scans at a scan rate of 100 mV s^{-1} within a range of 1.17–0.97 V vs RHE. Overpotential data were derived from the polarization curves recorded via linear sweep voltammetry (LSV) at 5 mV s^{-1} in the range of 0.97–1.72 V vs RHE. Additionally, the performance of the commercial catalyst, IrO_2, was evaluated. All the raw data were subjected to 67% iR correction during the analysis.

3.3 Result and Discussion

Material characterization

The X-ray diffraction (XRD) patterns of Fe-bIm, Fe-(bIm)0.3Caf, and Fe-Caf (**Figure 6**) comprise diffraction peaks (**Table 1**) corresponding to the (104), (110), (113), (024), (116), (122), (214), (300), (1010), (312), and (134) crystal planes of α-Fe_2O_3 (hematite), which is consistent with syn (JCPDS No. 089-0597). Additionally, an intense peak at approximately 22° indicates the presence of an exposed carbon skeleton.[23] These observations confirm that hematite nanocrystals are successfully prepared and functionalized with the functional groups in the carbon skeleton. Furthermore, Fe-Caf exhibited a lower crystalline state than that of Fe-bIm and Fe-(bIm)0.3Caf.

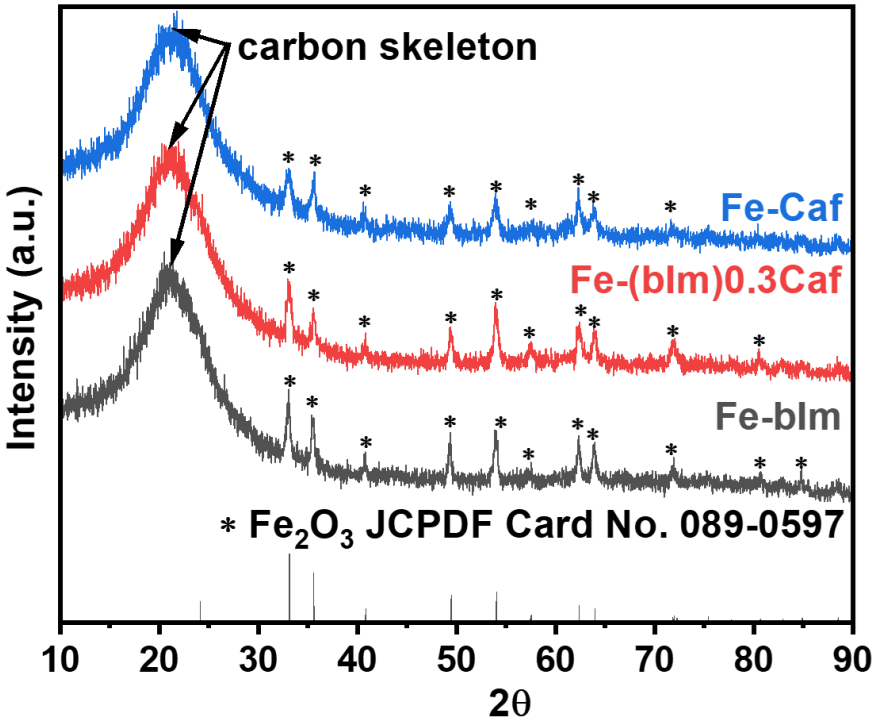

Figure 6. XRD patterns of Fe-bIm, Fe-(bIm)0.3Caf, Fe-Caf, and Fe_2O_3 (JCPDS No. 089-0597)

Table 1. List of Fe-bIm, Fe-(bIm)0.3Caf, and Fe-Caf diffractions and its phase name

Fe-bIm	Fe-bImCaf	Fe-Caf	Phase name	Chemical formula
33.02	33.06	33.02	Hematite, syn(1,0,4)	Fe_2O_3
35.48	35.54	35.63	Hematite, syn(1,1,0)	Fe_2O_3
40.69	40.83	40.88	Hematite, syn(1,1,3)	Fe_2O_3
49.25	49.33	49.38	Hematite, syn(0,2,4)	Fe_2O_3
53.91	53.89	53.92	Hematite, syn(1,1,6)	Fe_2O_3
57.27	57.40	57.6	Hematite, syn(2,1,4)	Fe_2O_3
62.50	62.40	62.55	Hematite, syn(1,2,5)	Fe_2O_3
63.84	63.93	63.89	Hematite, syn(3,0,0)	Fe_2O_3
71.72	71.88		Hematite, syn(1,0,10)	Fe_2O_3
80.71	80.56		Hematite, syn(1,2,8)	Fe_2O_3
84.75			Hematite, syn(1,3,4)	Fe_2O_3

All the samples were characterized as nanoparticles using field-emission scanning electron microscopy (FE-SEM) (**Figure 7**), and their elemental weight percentages (wt%) were analyzed via elemental mapping using energy dispersive X-ray spectroscopy (EDS) (**Figure 8–10**). All the samples were composed of nanoparticles with a uniform size distribution. Moreover, among the analyzed samples, Fe-(bIm)0.3Caf possessed the highest iron content of 78.25%, whereas Fe-bIm and Fe-Caf contained 76.48% and 61.46% of iron, respectively. Furthermore, the elemental mapping of all synthesized samples clearly revealed the surface functionalization of the carbon skeleton with uniformly distributed Fe_2O_3.

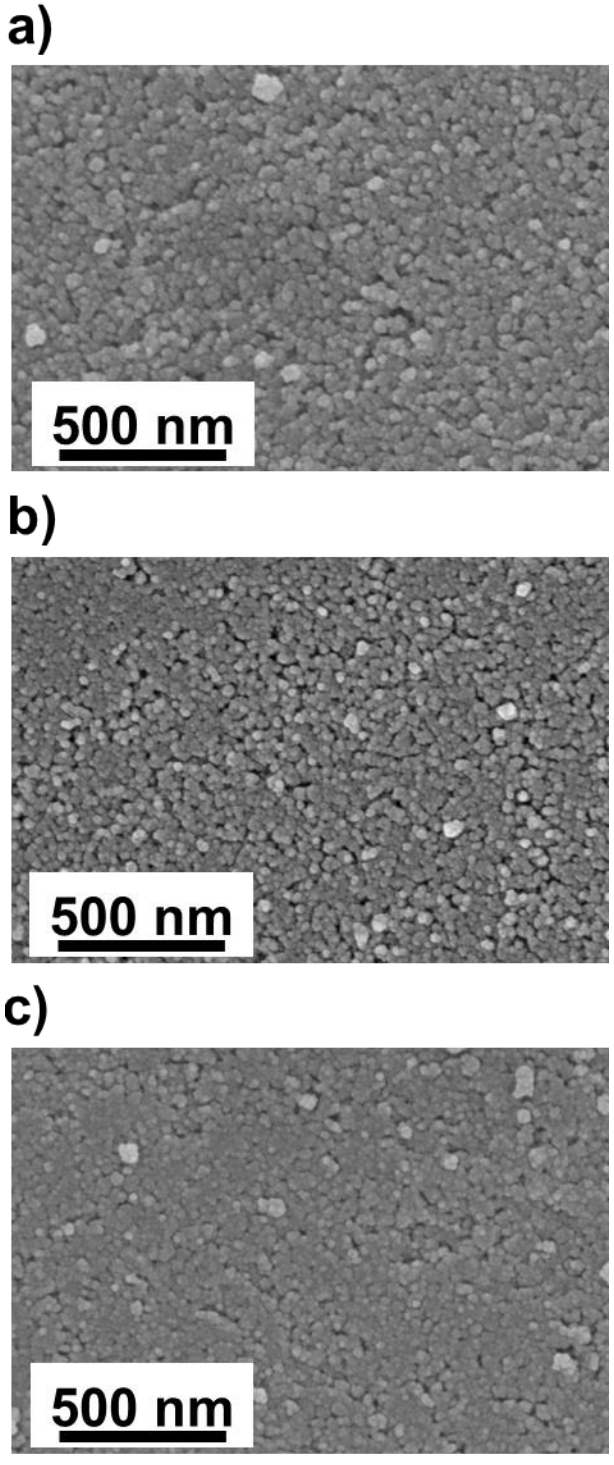

Figure 7. FE-SEM images of a) Fe-bIm, b) Fe-(bIm)0.3Caf, and c) Fe-Caf

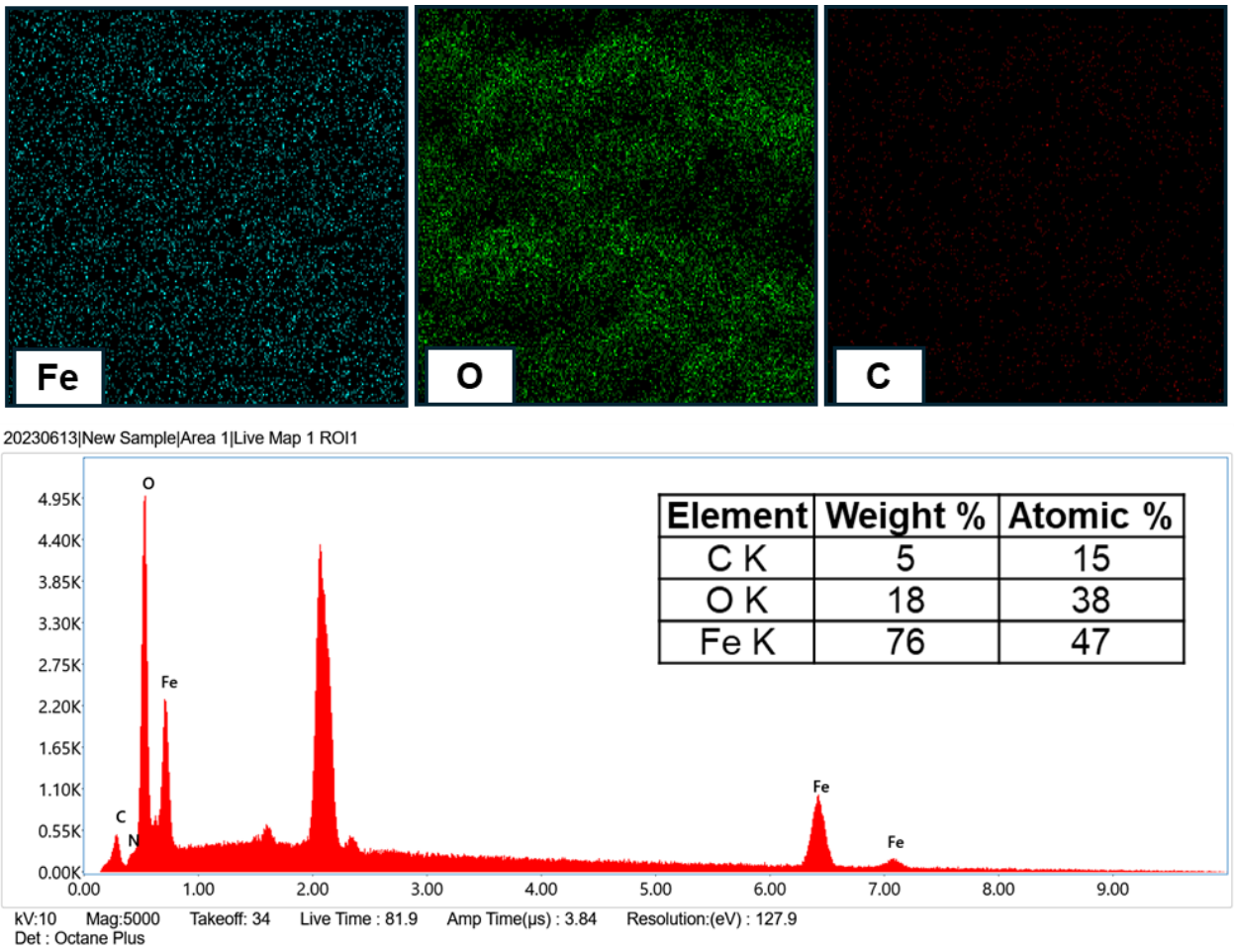

Element	Weight %	Atomic %
C K	5	15
O K	18	38
Fe K	76	47

Figure 8. EDS of Fe-bIm

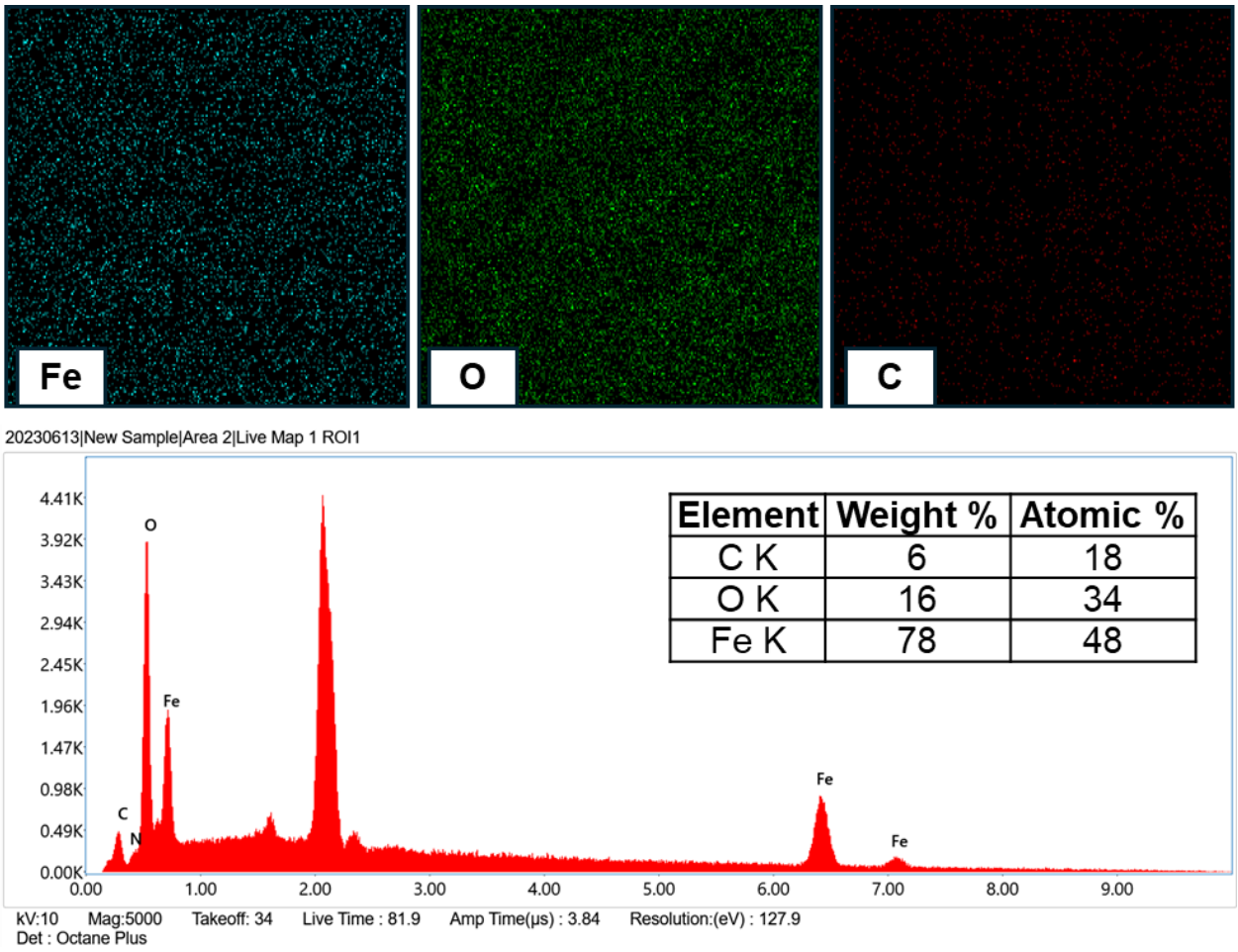

Element	Weight %	Atomic %
C K	6	18
O K	16	34
Fe K	78	48

Figure 9. EDS of Fe-(bIm)0.3Caf

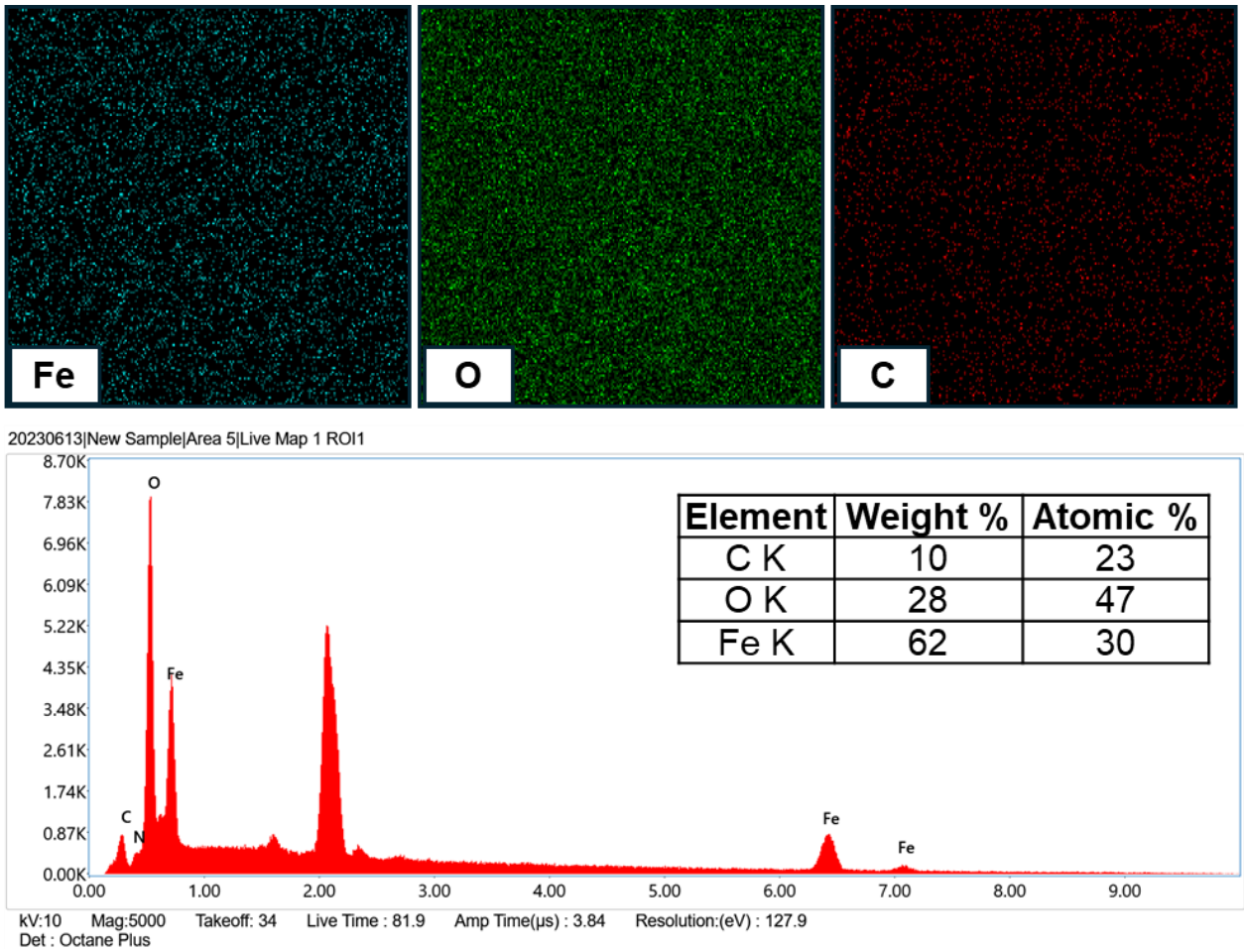

Element	Weight %	Atomic %
C K	10	23
O K	28	47
Fe K	62	30

Figure 10. EDS of Fe-Caf

The morphology, shape, size, and elemental distribution of Fe-(bIm)0.3Caf were further validated via high-resolution transmission electron microscopy (HR-TEM) in combination with EDS (**Figure 11**). HR-TEM images (**Figure 11a**) revealed the presence of hematite nanocrystals with two distinct shapes: sphere[26] and rhombohedron (cube-like particles).[27] The spherical nanoparticles observed in Fe-(bIm)0.3Caf possessed an average particle size of approximately 3 nm. Additionally, HR-TEM imaging conducted at a high magnification using a strong electron beam revealed discernible rhombohedral particles with nanoscale edge lengths (22 nm). Furthermore, the rhombohedral particles exhibited obtuse angles measuring 107°, which was consistent with previous reports.[28] In the region of the spherical hematite particles (**Figure 11b**), lattice fringes with an interlayer spacing of 0.186 nm, corresponding to the (024) plane, were observed. Conversely, in **Figure 11c,** an interlayer spacing of 0.268 nm is observed, and this value is consistent with that of the rhombic crystals enclosed by six (104) facets.[29] The material exhibited excellent crystallinity, as evidenced by the clear lattice structures. Furthermore, the elemental mapping images (**Figure 11d–f**) indicated the presence of Fe, O, and C atoms, as revealed by the EDS equipment integrated with FE-SEM. However, owing to the use of a high magnification and focused electron beam, HR-TEM analysis provided evidence for the presence of N elements, which were not discernible using FE-SEM (**Figure 11g**). This observation is consistent with the presence of hematite within the carbon skeleton, as indicated by XRD and elemental mapping analyses, which revealed a uniform distribution of C and N along with Fe and O. These findings indicate the surface engineering of hematite by a matrix of functional groups.

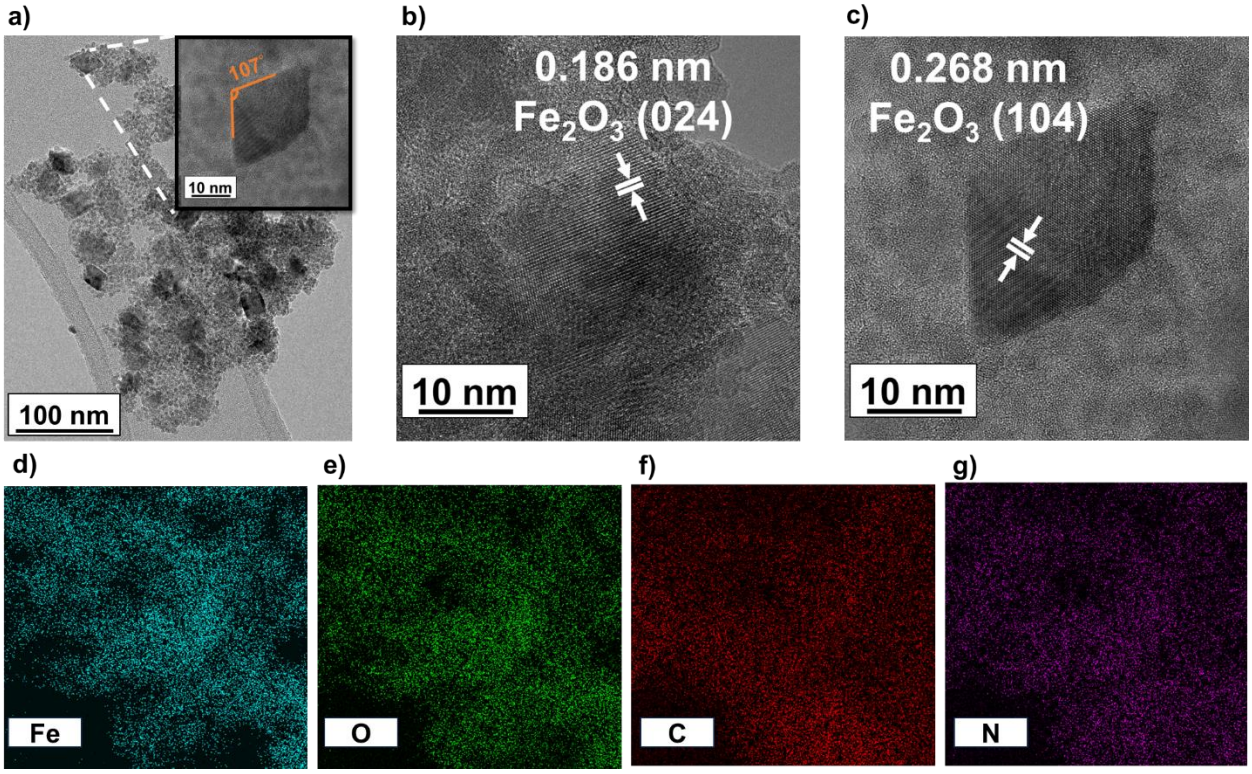

Figure 11. (a) HR-TEM image of interface-functionalized hematite nanocrystals. (b–c) Lattice fringes and (d–g) elemental mapping images of Fe-(bIm)0.3Caf

Fourier transform infrared (FT-IR) spectroscopy is a crucial technique to verify the presence of functional groups. Generally, all the three samples, Fe-bIm, Fe-(bIm)0.3Caf, and Fe-Caf, exhibited similar functional groups (**Figure 12**). The broad band in the range of 3000–3600 cm^{-1} with a peak centered at 3418 cm^{-1} corresponds to the stretching vibrations of the hydroxyl group (OH−) in the adsorbed water molecules.[30] Additionally, a peak corresponding to the uncoordinated free $–NH_2$ group was observed within the range of 3300–3500 cm^{-1}, and the band at 1555 cm^{-1} was ascribed to the bending vibration of $–NH_2$.[30, 31] Moreover, the bands at 1737 and 1046 cm^{-1} are assigned to the C=O and C−O stretching vibrations of the carboxylic acid group, respectively.[32] Furthermore, the peaks at 1616 and 1389 cm^{-1} are attributed to the symmetric and asymmetric stretching of the carboxylate group (COO−), respectively.[33] The characteristic peaks of Fe−O stretching were observed at 575 and 471 cm^{-1}, corresponding to α-Fe_2O_3,[34] which was consistent with the XRD results. These observations strongly indicate the successful preparation of interface-functionalized hematite nanocrystals.

The thermogravimetric analysis of Fe-(bIm)0.3Caf pyrolysis conducted under a constant nitrogen flow reveals a mass loss below 100°C due to the evaporation of excess water and solvents (**Figure 13**). At high temperatures (≥600°C), a significant weight loss occurs primarily because of the removal of functional groups, such as hydroxyl and carboxylate groups as well as amine and aromatic rings, which is consistent with the FT-IR results. In the range of 600°C–900°C, the weight of Fe-(bIm)0.3Caf remains approximately constant with increasing temperature, indicating the presence of Fe_2O_3 in the composite structure, which reaffirms the XRD and HR-TEM results.

The corresponding nitrogen adsorption–desorption profiles of Fe-bIm, Fe-(bIm)0.3Caf, and Fe-Caf are presented in **Figure 14**. Furthermore, the Brunauer–Emmett–Teller (BET) surface area of the samples was analyzed. In this study, Fe-(bIm)0.3Caf exhibits the largest specific surface area of 143.46 $m^2\ g^{-1}$, which is larger than that of Fe-bIm (124.49 $m^2\ g^{-1}$) and Fe-Caf (69.72 $m^2\ g^{-1}$). This advantage of a larger surface area implies that the mixed-ligand sample will have a higher exposure to electrolytes, enhancing the electrochemical activity.

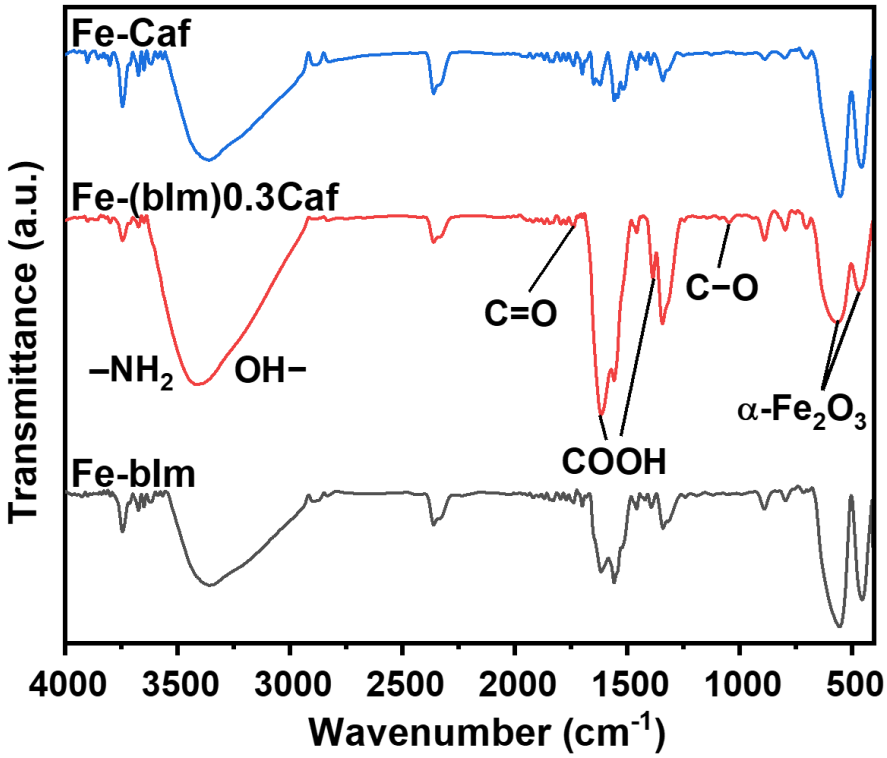

Figure 12. FT-IR spectra of Fe-bIm, Fe-(bIm)0.3Caf, and Fe-Caf

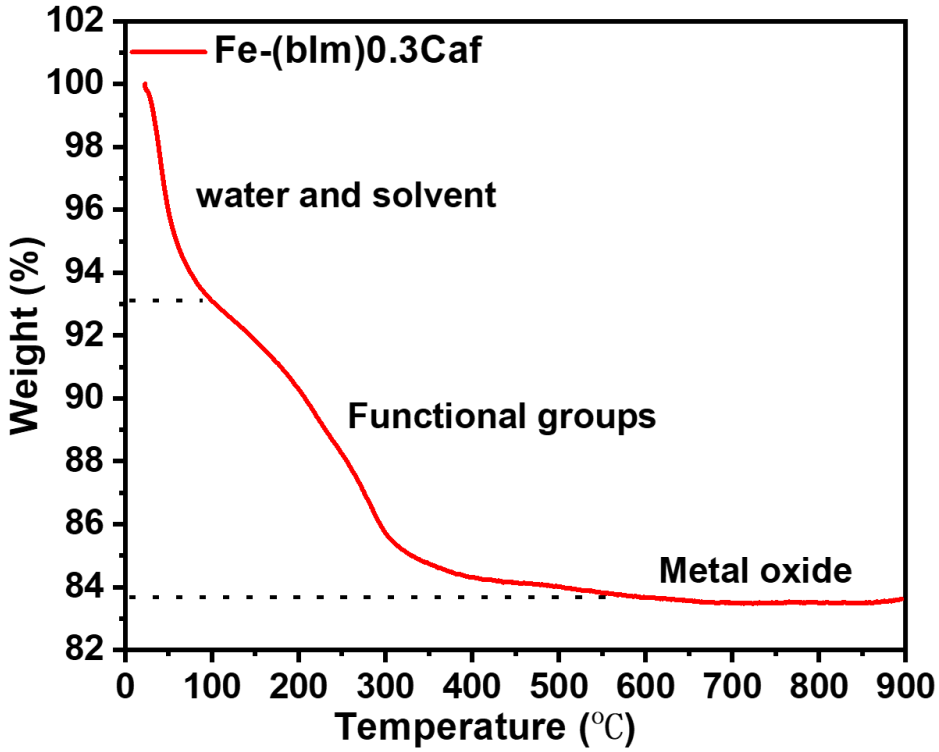

Figure 13. TGA curve of Fe-(bIm)0.3Caf

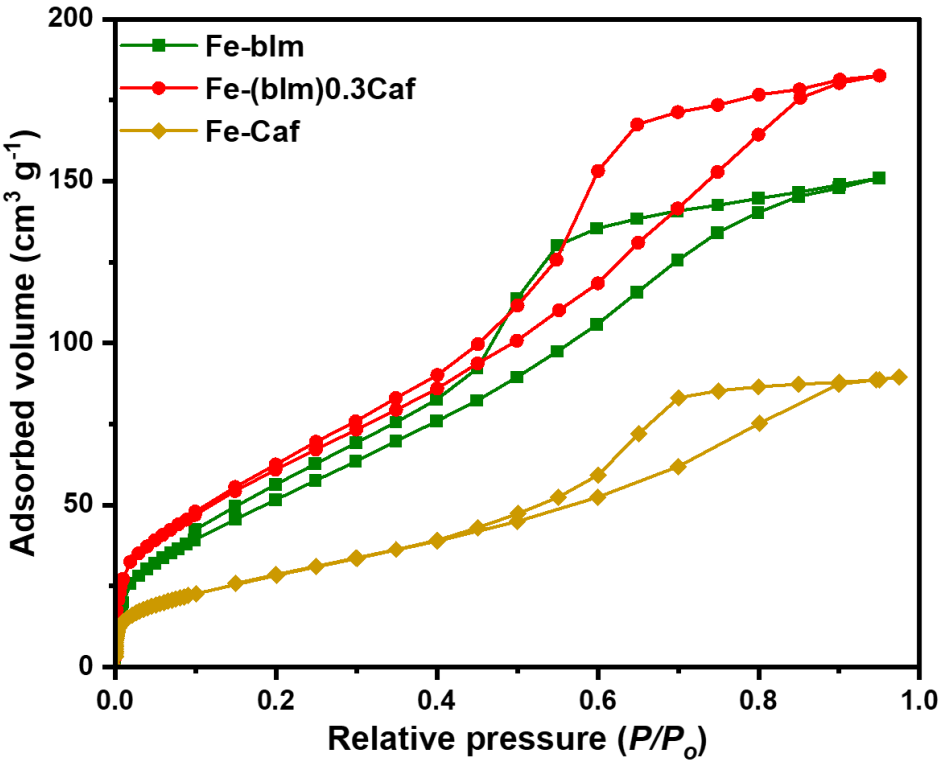

Figure 14. BET surface area of Fe-bIm, Fe-(bIm)0.3Caf, and Fe-Caf

The Raman spectra (**Figure 15**) revealed insights into the disorder within the crystal lattice of hematite Fe-(bIm)0.3Caf and commercial Fe_2O_3. For Fe-(bIm)0.3Caf, the peaks observed at 216 and 485 cm^{-1} are attributed to the A_{1g} mode, whereas the peaks at 281, 395, and 599 cm^{-1} are assigned to the E_g mode. Similarly, the Fe_2O_3 spectrum displays characteristic peaks at 218 (A_{1g}), 286 (E_g), 400 (E_g), 496 (A_{1g}), and 595 cm^{-1} (E_g).[35] Moreover, the extraneous peaks at 642 and 644 cm^{-1} in the spectra of Fe-(bIm)0.3Caf and commercial Fe_2O_3, respectively, are indicative of disorder within the crystal lattice.[36, 37] Furthermore, the peaks observed at 1296 and 1310 cm^{-1} for hematite and Fe_2O_3, respectively, originate from the second-order scattering processes, specifically the two-phonon or two-magnon scattering processes.[38, 39] Therefore, Raman analysis corroborates the XRD and FT-IR findings, confirming that Fe_2O_3 exists as α-Fe_2O_3 in Fe-(bIm)0.3Caf.

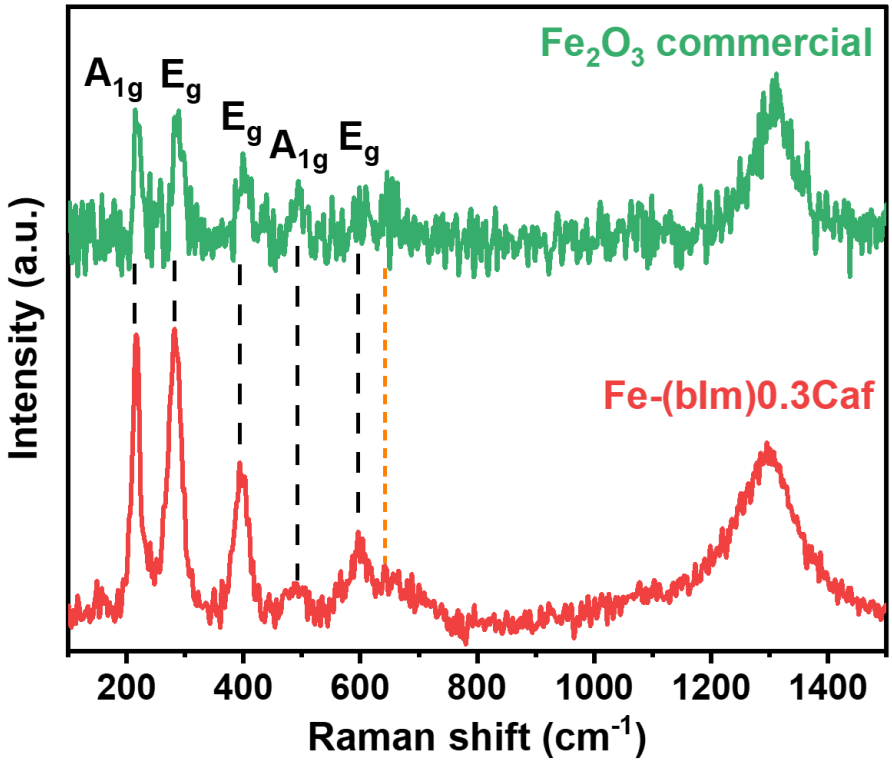

Figure 15. Raman spectra of Fe-(bIm)0.3Caf and commercial Fe_2O_3

Electron paramagnetic resonance (EPR) offers crucial insights into the unpaired electrons present in materials. Oxygen-vacancy-containing materials may possess unpaired electrons, and the content of oxygen vacancies can influence the strength of the EPR signal. Oxygen vacancies play a significant role in OER activity, affecting the intermediate adsorption on the electrocatalyst surface, modifying the electronic structure, and enhancing the conductivity.[18] **Figure 16** illustrates a significantly heightened EPR signal intensity at g = 2.003 for Fe-(bIm)0.3Caf, indicating abundant oxygen vacancies. In contrast, the Fe-bIm and Fe-Caf samples did not yield any signals, indicating the absence of oxygen vacancies.[40] Notably, defects resulting from the substitution of the second ligand, Caf, in the mixed-ligand sample can induce defects in MOs, leading to the formation of oxygen vacancies, which enhance the OER activity.

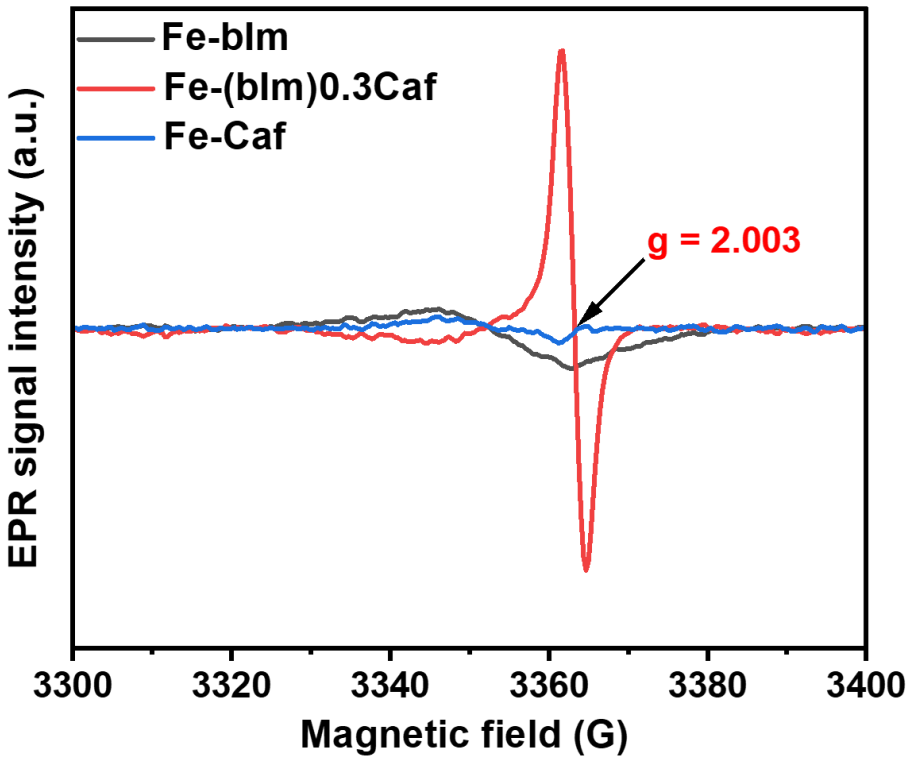

Figure 16. EPR spectra of Fe-bIm, Fe-(bIm)0.3Caf, and Fe-Caf

The surface valence and bonding conFigureurations were evaluated via X-ray photoelectron spectroscopy (XPS) to determine the presence of Fe 2p, C 1s, and O 1s in Fe-bIm, Fe-(bIm)0.3Caf, and Fe-Caf (**Figure 17**). The deconvolution of the Fe 2p spectrum (**Figure 17a**) revealed distinct peaks corresponding to Fe $2p_{3/2}$ (Fe^{2+} = 709.58 eV and Fe^{3+} = 711.73 eV) and Fe $2p_{1/2}$ (Fe^{2+} = 723.13 eV and Fe^{3+} = 725.75 eV) for Fe-(bIm)0.3Caf. Additionally, the satellite peaks of Fe $2p_{3/2}$ and Fe $2p_{1/2}$ were observed at 717.17 and 730.69 eV, respectively.[41] Similarly, the Fe-bIm spectrum exhibited small peaks of Fe $2p_{3/2}$ (Fe^{2+} = 708.72 eV and Fe^{3+} = 711.16 eV) and Fe $2p_{1/2}$ (Fe^{2+} = 722.37 eV and Fe^{3+} = 725.39 eV), whereas the Fe-Caf spectrum comprised peaks of Fe $2p_{3/2}$ (Fe^{2+} = 708.38 eV and Fe^{3+} = 711.02 eV) and Fe $2p_{1/2}$ (Fe^{2+} = 721.69 eV and Fe^{3+} = 724.52 eV). The analysis based on Fe 2p data deconvolution implied the presence of both ferrous and ferric states, corroborating the oxidation state of Fe_2O_3, as confirmed by the XRD, FT-IR, and Raman analyses. The positive shifts of the Fe 2p binding energy compared to Fe-bIm and Fe-Caf during the deconvolution process for Fe-(bIm)0.3Caf imply an elevated oxidation degree of the Fe species.[42, 43] This increase in the oxidation state is anticipated to result in high activity during OER catalysis.[44] The C 1s XPS spectra (**Figure 17b**) of Fe-bIm and Fe-(bIm)0.3Caf comprised multiple peaks, whereas the Fe-Caf spectrum displayed three peaks. The Fe-(bIm)0.3Caf spectrum exhibited peaks at 283.76 (metal carbide), 284.55 (C−C), 286.29 (C−O−C), and 288.00 eV (O−C=O), indicating that all deconvolutionpeaks shift to higher binding energies compared with the Fe-bIm spectrum, which comprised peaks at 283.47 (metal carbide), 284.66 (C−C), 286.81 (C−O−C), and 288.40 eV (O−C=O). Conversely, the Fe-Caf spectrum displayed peaks at 282.52 (metal carbide), 284.08 (C−C), and 286.40 eV (C−O−C) without the presence of an O−C=O peak.[45, 46] The atomic ratio between O−C=O and C−O−C obtained for Fe-(bIm)0.3Caf was 0.87, which was higher than that of Fe-bIm (0.17), indicating the more prominent presence of O−C=O groups in Fe-(bIm)0.3Caf. This finding suggests that Fe-(bIm)0.3Caf is expected to demonstrate superior activity compared to that of the other analyzed samples owing to the positive correlation between the O−C=O-type groups and OER activity.[47] A larger proportion of the O−C=O component is essential for achieving higher OER activity of the mixed-ligand sample Fe-(bIm)0.3Caf compared to single-ligand

sample Fe-bIm. In the O 1s spectrum (**Figure 17c**), peaks corresponding to MOs, metal carbonate, and O−H were identified at 527.93, 529.19, and 532.09 eV for Fe-bIm and 527.03, 529.36, and 531.14 eV for Fe-Caf, respectively.[48, 49] In the case of Fe-(bIm)0.3Caf, a positive shift was observed for the peaks associated with MOs (528.40 eV) and metal carbonate (529.31 eV); however, the binding energy of the O−H peak (531.38 eV) was lower than that observed for Fe-bIm.

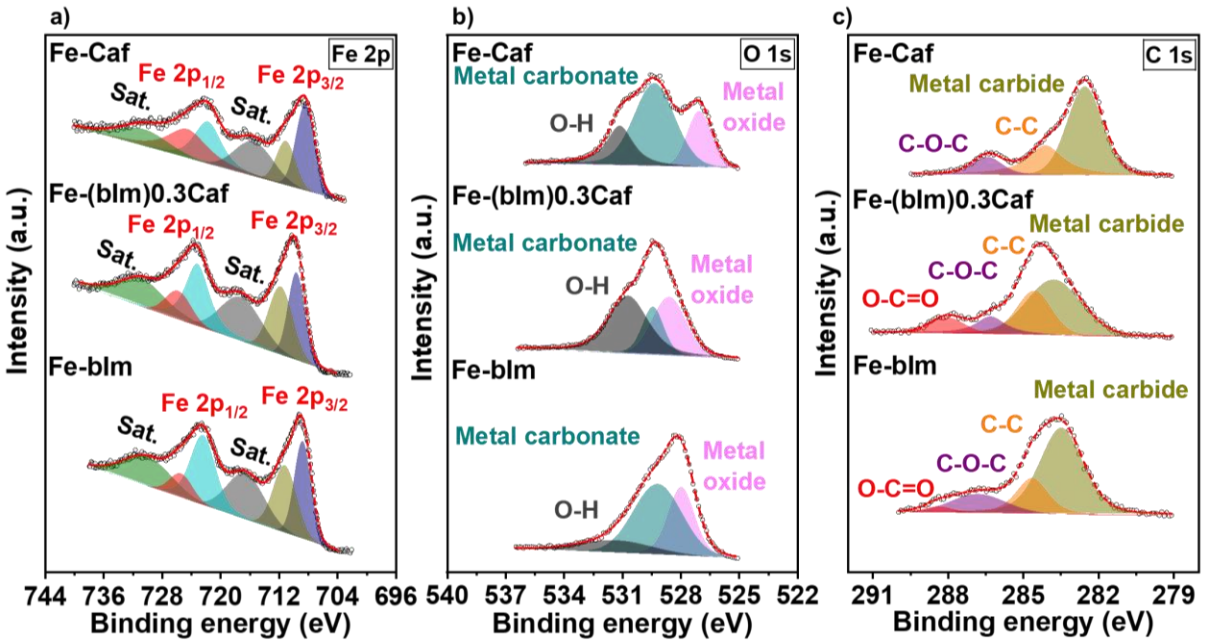

Figure 17. High-resolution XPS spectra of a) Fe 2p b) C 1s, and c) O 1s for Fe-bIm, Fe-(bIm)0.3Caf, and Fe-Caf

Electrocatalytic performance of interface-functionalized hematite the toward OER

From **Figure 18a**, at a low current density of 10 mA cm^{-2} (η_{10}), the mixed-ligand sample, Fe-(bIm)0.3Caf, exhibits the smallest overpotential of 264 mV, compared with Fe-bIm (272 mV), Fe-Caf (288 mV), and IrO_2 (280 mV). Additionally, at a higher current density of 100 mA cm^{-2} (η_{100}), Fe-(bIm)0.3Caf demonstrated a significantly lower overpotential of 292 mV, compared with Fe-bIm, Fe-Caf, and IrO_2, which exhibited the overpotentials of 314, 344, and 402 mV, respectively. Moreover, in the LSV analysis of all the samples, Fe-(bIm)0.3Caf demonstrated the largest improvement in current density, indicating its superior electrocatalytic properties. This enhancement can be attributed to the defects in the MOs in Fe-(bIm)0.3Caf, leading to the creation of oxygen vacancies, which play a crucial role in the adsorption of intermediates on the catalyst surface.[18] This is particularly beneficial for OH^- adsorption in the electrolyte solution during OER,[50] along with the enhancement of electronic transfer[51] and conductivity.[18] From another perspective, Caf substitution in bIm increased the content of the electron-withdrawing group (COO−), which has been reported to exhibit a positive correlation with OER activity.[47] This analysis demonstrated the effectiveness of the mixed-ligand strategy in increasing the OER activity.

Besides, the effects of Fe-(bIm)0.3Caf are the primary explanation for the smallest value among all synthesized samples in the Tafel slope obtained from the LSV curves (**Figureure 18b**) when evaluating the OER kinetics. Clearly, Fe-(bIm)0.3Caf exhibited the smallest Tafel slope of 30 mV dec^{-1}, which was significantly lower than the slopes obtained for Fe-bIm (40 mV dec^{-1}), Fe-Caf (51 mV dec^{-1}), and IrO_2 (91 mV dec^{-1}). These results indicate that Fe-(bIm)0.3Caf could achieve more favorable OER kinetics than the other analyzed samples.[52] A comparison of the overpotential and Tafel slope data of the interface-functionalized hematite nanocrystals and previously reported Fe-based electrocatalysts is presented in **Table 2**.

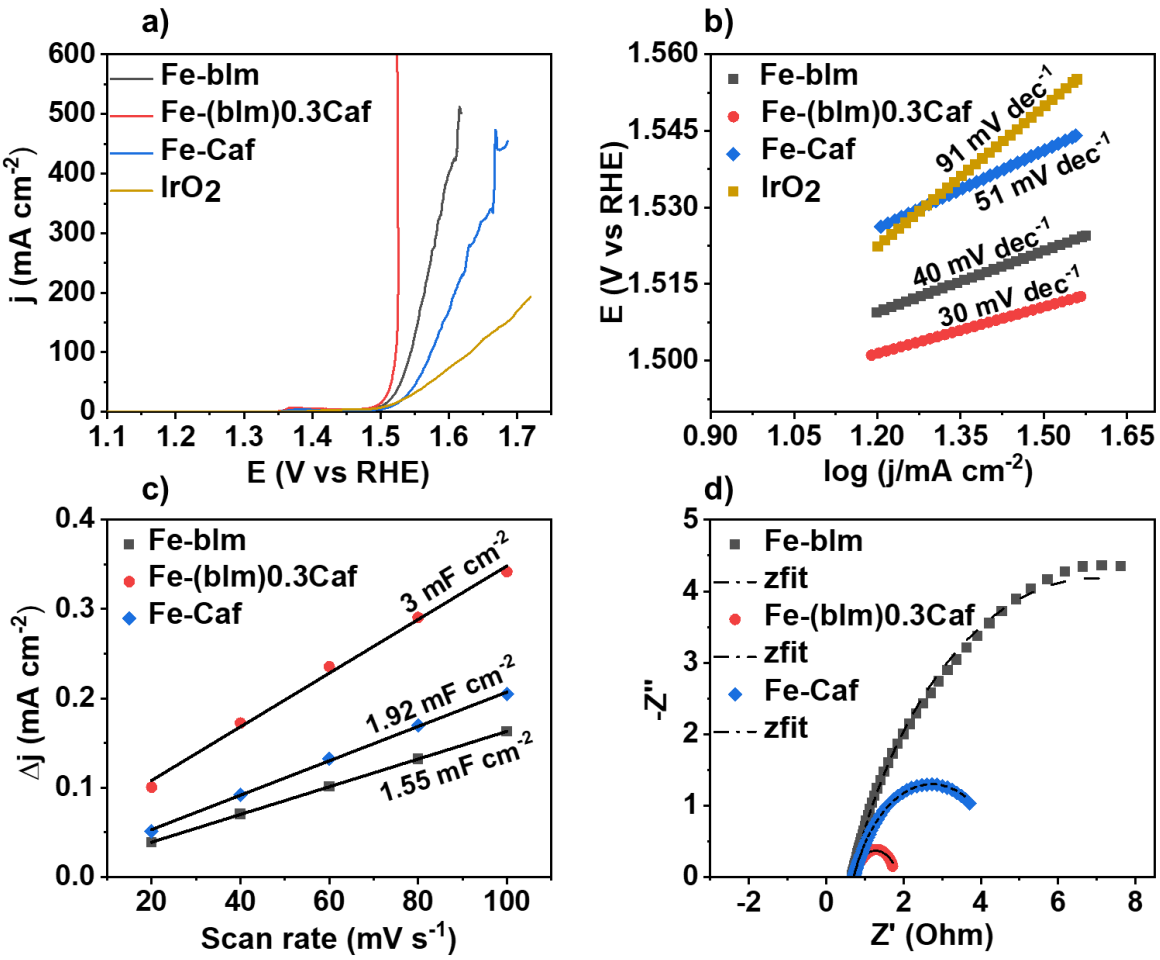

Figure 18. OER activity of all the samples. a) LSV polarization curve, b) Tafel slope, c) electrochemically active surface area (ECSA), and d) electrochemical impedance spectroscopy (EIS) results

Table 2. Comparison of the sample prepared in this study with previously reported iron-based electrocatalysts

Electrocatalyst	Electrolyte	Overpotential (mV) at 10 m cm^{-2}	Tafel slope ($mV\ dec^{-1}$)	Reference
Fe_2O_3@CNT	1 M KOH	270	45	[53]
Co-Fe_2O_3	1 M KOH	322	76	[54]
Mn-Fe_2O_3	1 M KOH	351	102	[54]
Ni-Fe_2O_3	1 M KOH	285	62	[54]
$Co_{0.5}Fe_{0.5}WO_4$-CNT	1 M KOH	290	42	[55]
Co-0.3 g $FeCoTe_2$-200	1 M KOH	300	36.99	[56]
Fe_2B NWs/NF	1 M KOH	276	30	[57]
NiOOH/Fe_2O_3	1 M KOH	325	-	[58]
Fe_2O_3-MnO/NF	1 M KOH	370	66	[59]
α-Fe_2O_3@g-C3N4 NCs	1 M KOH	425	280	[60]
Fe_2O_3@GS	1 M KOH	510	98.11	[61]
Fe_3C NPs@NP-CNT-800	1 M KOH	280	45	[62]
Fe-(bIm)0.3Caf	1 M KOH	264	30	This work

The ECSA was analyzed by determining the double-layer capacitance, C_{dl}, using CV (**Figure 18c**). As expected, Fe-(bIm)0.3Caf displayed a distinctly highest value of C_{dl} (3.00 mF cm^{-2}), suggesting that Fe-(bIm)0.3Caf, owing to its largest BET surface area, could expose the most effective active sites.[63] The EIS results illustrated in **Figure 18d** provide further evidence to support this conclusion. Considering the Nyquist plots of all the samples, the smallest semicircular diameter was observed for Fe-(bIm)0.3Caf at a potential of 1.5 V, revealing the lowest charge-transfer resistance (R_{ct}) of 0.88 Ω. This indicates that the electron-transfer capability of Fe-(bIm)0.3Caf is the strongest compared to other synthesized samples. The C_{dl} and R_{ct} values summarized in **Table 3** suggest enhanced electron-transport properties, which the highest electrocatalytic activity belonging to Fe-(bIm)0.3Caf sample.[64]

Table 3. Double-layer capacitance C_{dl} and charge-transfer resistances R_{ct}

OER	Fe-(bIm)	Fe-(bIm)@Caf	Fe-Caf
double-layer capacitance C_{dl} (mF cm^{-2})	1.55	3.00	1.92
charge-transfer resistance R_{ct} (Ω)	6.59	0.88	2.64

Figure 19a presents a comparison of the LSV polarization curves of the optimal sample obtained in this study, Fe-(bIm)0.3Caf, with commercial Fe_2O_3, clearly demonstrating the superior OER activity of Fe-(bIm)0.3Caf, which exhibits significantly lower overpotentials. Commercial Fe_2O_3 required 331 mV to reach a current density of 10 mA cm^{-2}, whereas Fe-(bIm)0.3Caf needed only 264 mV to attain the same current density, emphasizing the crucial role of oxygen vacancies in the hematite composite catalyst. Furthermore, at 100 cm^{-1}, Fe-(bIm)0.3Caf exhibited an overpotential of 292 mV, which was significantly lower than the corresponding value obtained for commercial Fe_2O_3 (434 mV). Fe-(bIm)0.3Caf possesses heteroatoms N in the carbon skeleton, which interact with metal and cause alterations in the interfacial electronic transfer and charge distribution. This interaction mitigates the issue of the low conductivity in hematite. Moreover, the high electronegativity of heteroatoms N and O in various functional groups results in stronger MSIs compared to single oxides in commercial Fe_2O_3, leading to the formation of covalent bonds between metals and the carbon skeleton. This increases the electron transfer rate and conductivity, contributing to higher OER performance of Fe-(bIm)0.3Caf compared to commercial Fe_2O_3. Compared with commercial Fe_2O_3, Fe-(bIm)0.3Caf exhibited MSIs owing to the surface engineering with diverse functional groups. This MSIs effect can alter the OER mechanism by inducing changes in the electronic and geometric structures. As the covalence of the M–O bond increases because of the MSIs effects, the reaction mechanism tends to shift from the AEM to LOM, which has a theoretical overpotential of <0.37 V, resulting in an improved OER activity.[19] Additionally, interface functionalization enhances the electronic structure of the electrocatalyst, promoting the mass transfer and exposing more number of active sites, which enhance the OER activity.[42, 65] Moreover, electron-withdrawing (–COOH) and electron-donating ($–NH_2$) groups are notable for their effects on the OER performance of Fe-(bIm)0.3Caf compared to commercial Fe_2O_3. A high density of $–NH_2$ donates electrons to combine with H^+ ions, whereas –COOH absorbs electrons to combine with OH^- ions, contributing to increase the OER electrocatalytic activity. Furthermore, surface functionalization can result in the incorporation of heteroatoms, including oxygen and nitrogen, into the carbon skeleton, which can regulate the electronic structure of catalysts, coordinating the

MSIs between metals and the functional groups in the metal phase that connects with the functional groups. Functional groups raising strong interaction can regulate electronic and geometric structures, enhancing the catalytic performance.[19] In the interface-functionalized mixed-ligand sample, Fe-(bIm)0.3Caf, the issue of the low conductivity of Fe_2O_3 is mitigated through the introduction of the oxygen vacancies and heteroatoms.

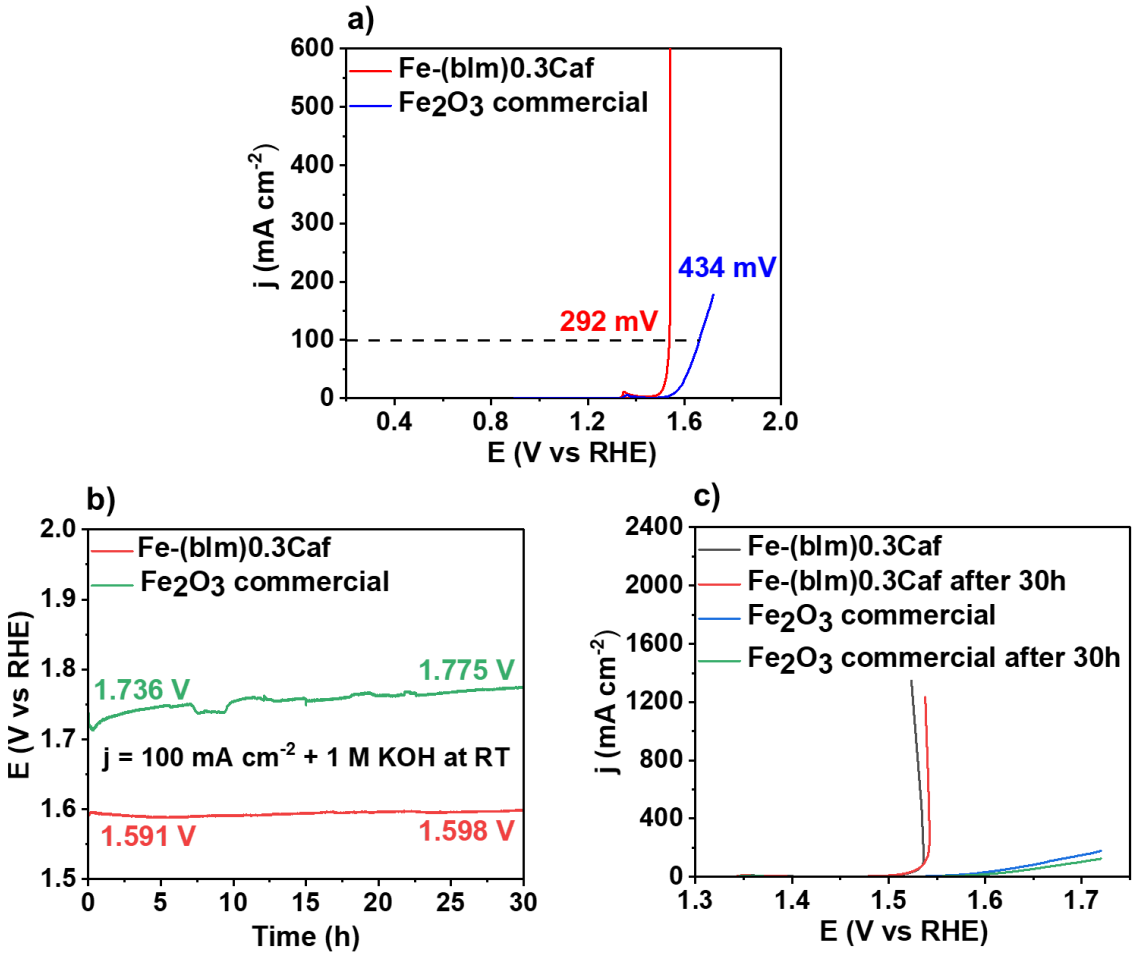

Figure 19. Comparison of the OER activity of Fe-(bIm)0.3Caf and commercial Fe_2O_3. a) LSV polarization curves, b) CP (E–t) test, and c) LSV polarization curves before and after the stability test

Additionally, Fe-(bIm)0.3Caf exhibited high durability in the chronopotentiometry (CP) test for 30 h (**Figure 19b)**. A slight increase in the measured potential was observed at 10 mA cm^{-2} for Fe-(bIm)0.3Caf, whereas a significant increasing tendency of potential was noted for commercial Fe_2O_3 (1.736–1.775 V), along with an activity retention of 97.75%. These observations indicate the higher durability of Fe-(bIm)0.3Caf compared to commercial Fe_2O_3, with the activity retention remaining considerably high at 99.57% within the voltage range of 1.591–1.598 V. Additionally, the LSV polarization curves obtained after 30 h were analyzed to compare the durability of Fe-(bIm)0.3Caf and Fe_2O_3 (**Figure 19c**). The results were consistent with those of the stability test, with Fe-(bIm)0.3Caf displaying almost similar trends as those observed in the LSV analysis. However, commercial Fe_2O_3 exhibited an ultrahigh overpotential at low currents. Despite the improvement in OER activity resulting from the transition of the mechanism from the AEM to LOM, the involvement of lattice oxygen and formation of highly under-coordinated sites during OER frequently lead to issues related to catalyst reconstruction and instability.[9] Owing to the MSIs effects, Fe-(bIm)0.3Caf can stabilize metal compounds and enhance the covalent characteristics of the M−O bond, maintaining a balance between the two reaction mechanisms to ensure the stability and efficiency of catalysts.[19]

Figure 20 illustrates a comparison of Fe-(bIm)0.3Caf and commercial Fe_2O_3 before and after the stability test via FE-SEM images. Fe-(bIm)0.3Caf displayed minimal changes after 30 h of stability testing, maintaining its spherical particle morphology (**Figure 20a and b**). Conversely, the commercial sample initially exhibited large particle sizes, and after the stability test, the particles lost their shape and became more conglomerated, and the sample exhibited a shift toward a bulk shape (**Figure 20c and d**). Morphology significantly influences catalyst performance; the bulk morphology observed after the stability test of commercial Fe_2O_3 further constrains the catalyst's ability to generate oxygen due to the material's tendency to impede the release of oxygen gas as the catalyst's contact area with the electrolyte diminishes.[66] Additionally, Fe-(bIm)0.3Caf offered a robust interaction between the metal species and the carbon skeleton matrix, inhibiting metal aggregation and increasing the electrocatalyst stability. This analysis reaffirms that interface functionalization can enhance both the activity and stability of hematite, emphasizing the efficacy of surface engineering strategies in augmenting the OER activity in alkaline media.

Additionally, the Fe content (**Figure 21–23**) in both Fe-(bIm)0.3Caf and Fe_2O_3 decreased after the stability test, compared with the initial measurements, suggesting sample loss during the stability test as indicated by the EDS analysis.

Following durability evaluation, the XRD patterns of Fe-(bIm)0.3Caf before and after the test were compared, as shown in **Figure 24**.After the durability test, all the initially observed hematite peaks were present, with the additional appearance of FeOOH peaks at 34.36° and 60.87°..[67] This result indicates the oxidation of Fe^{2+} to Fe^{3+} during the test.

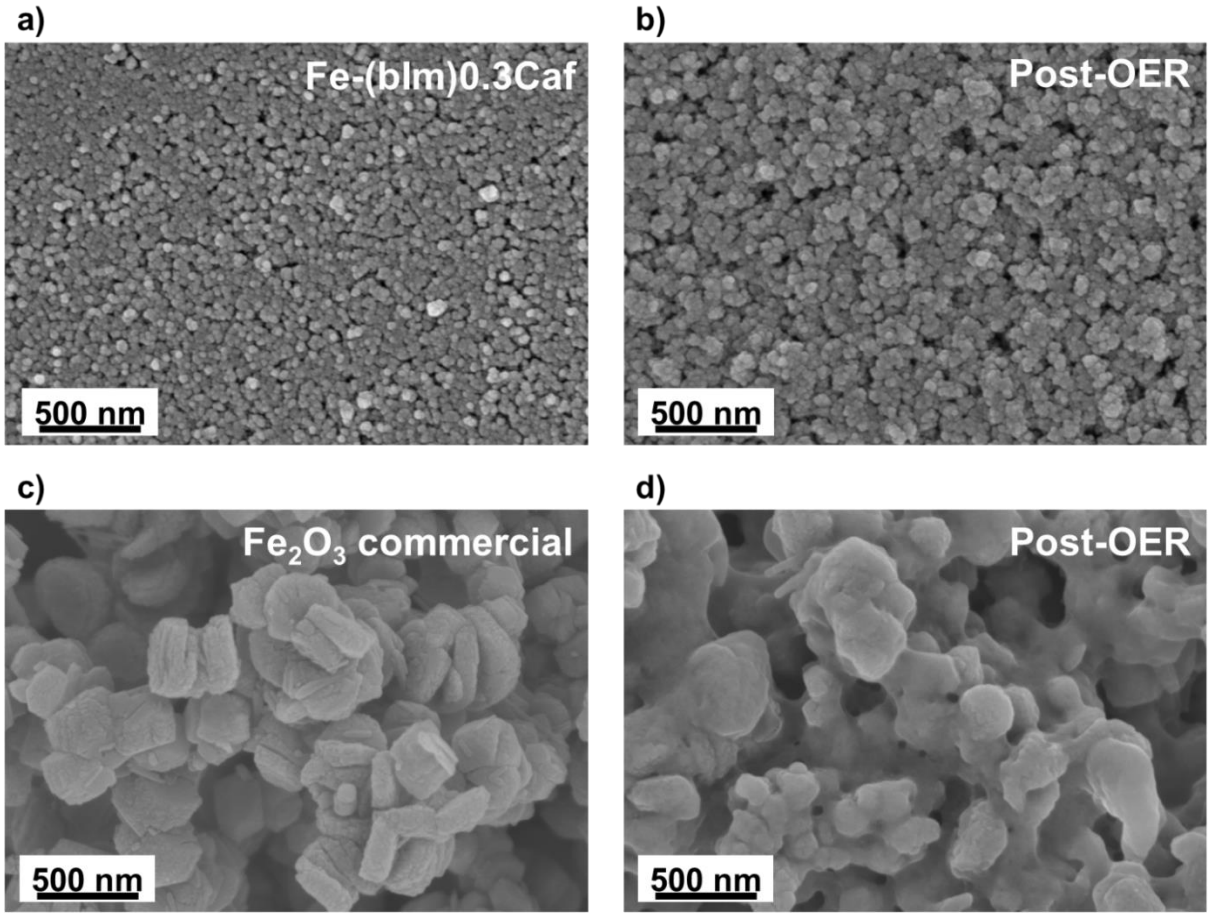

Figure 20. FE-SEM images morphologies of Fe-(bIm)0.3Caf and commercial Fe_2O_3 after the stability test

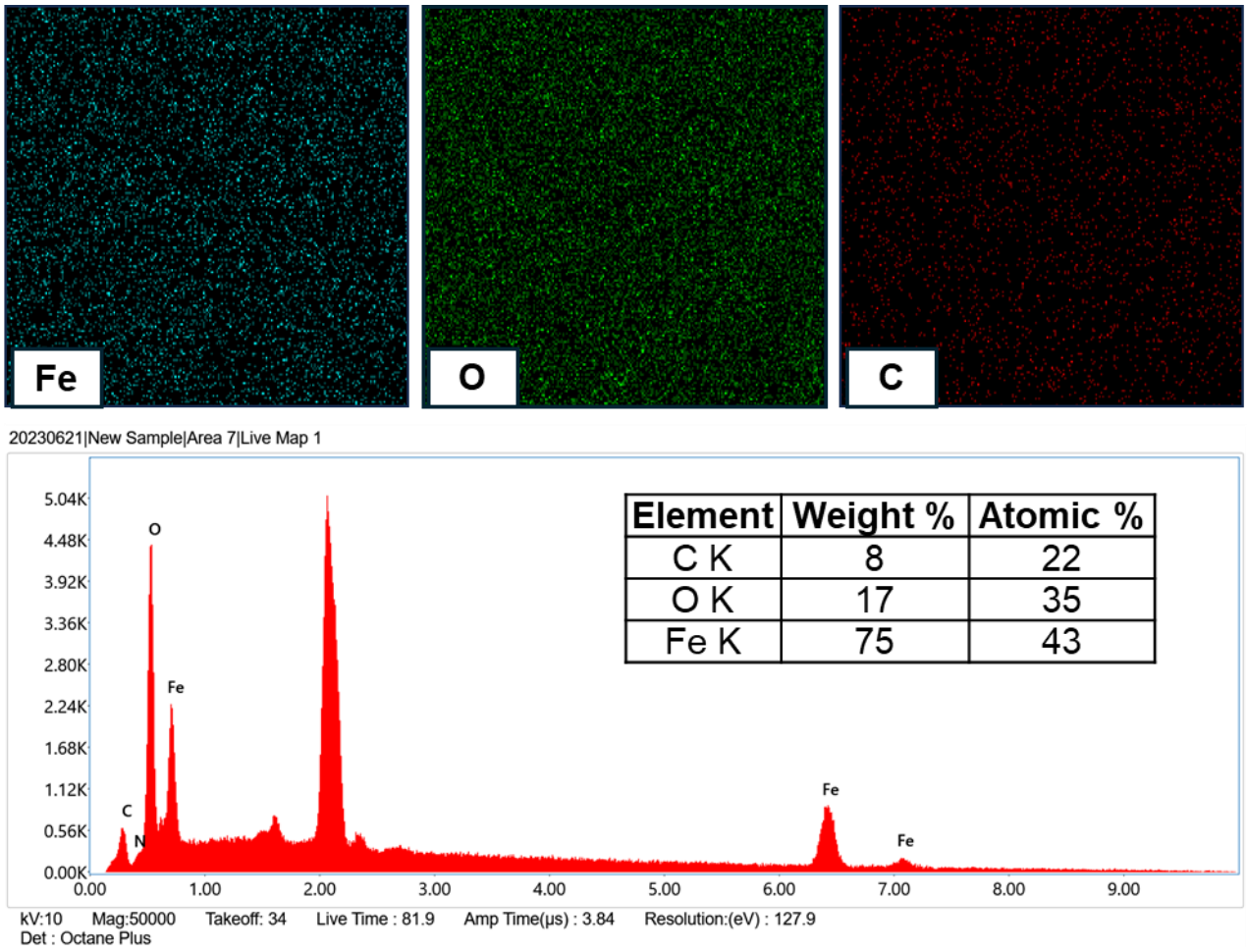

Element	Weight %	Atomic %
C K	8	22
O K	17	35
Fe K	75	43

Figure 21. EDS of Fe-(bIm)0.3Caf after stability test

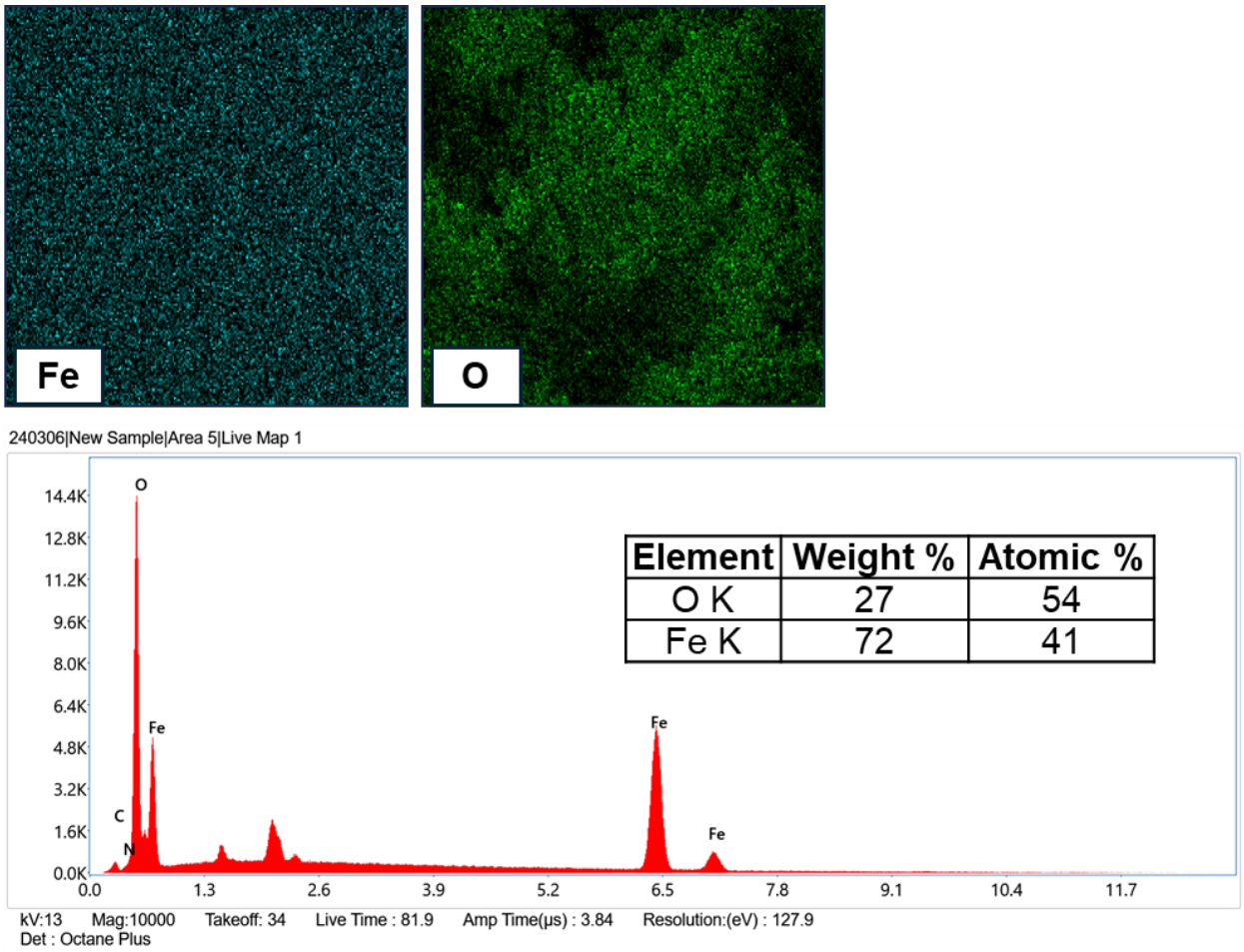

Figure 22. EDS of commercial Fe_2O_3

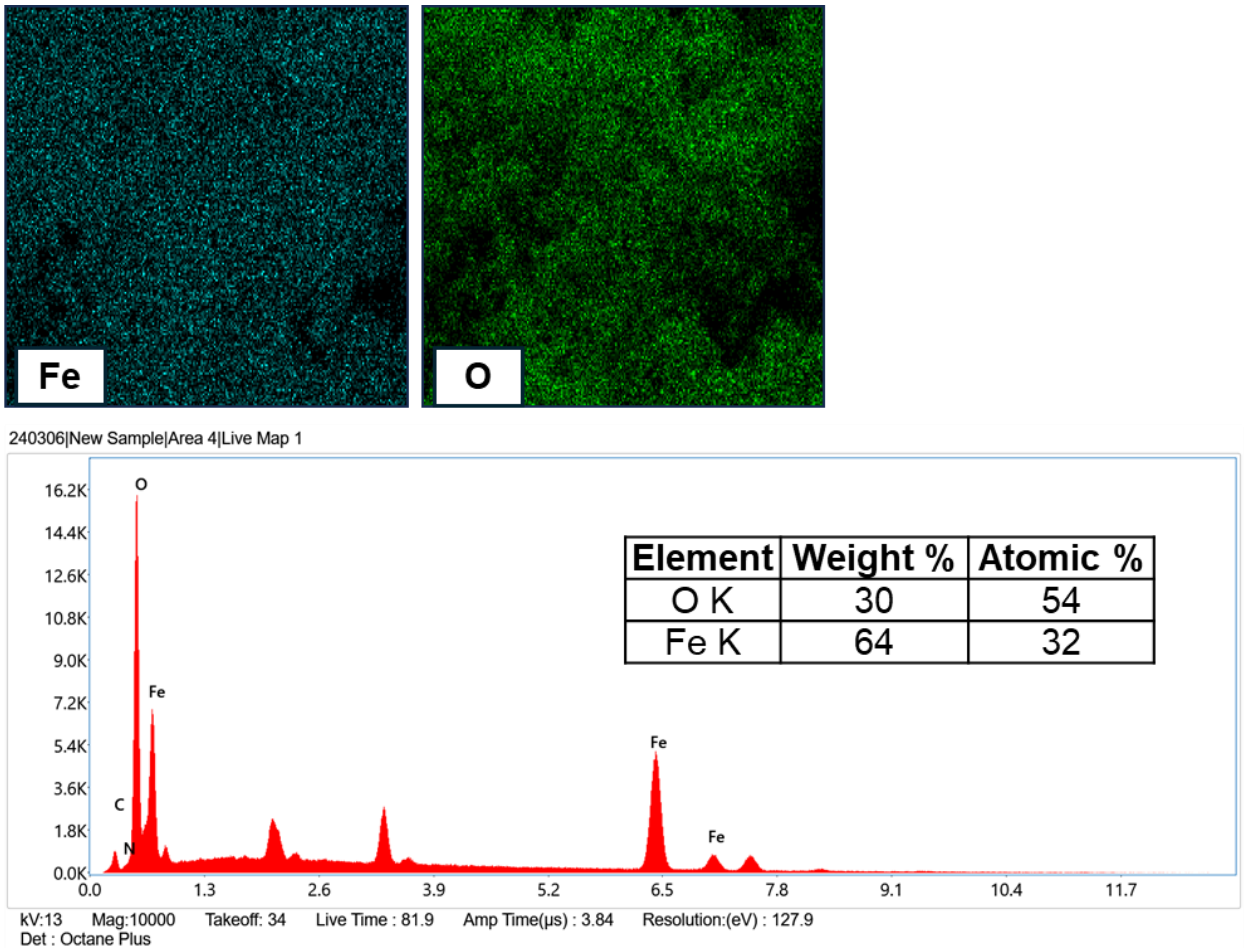

Figure 23. EDS of commercial Fe_2O_3 after stability test

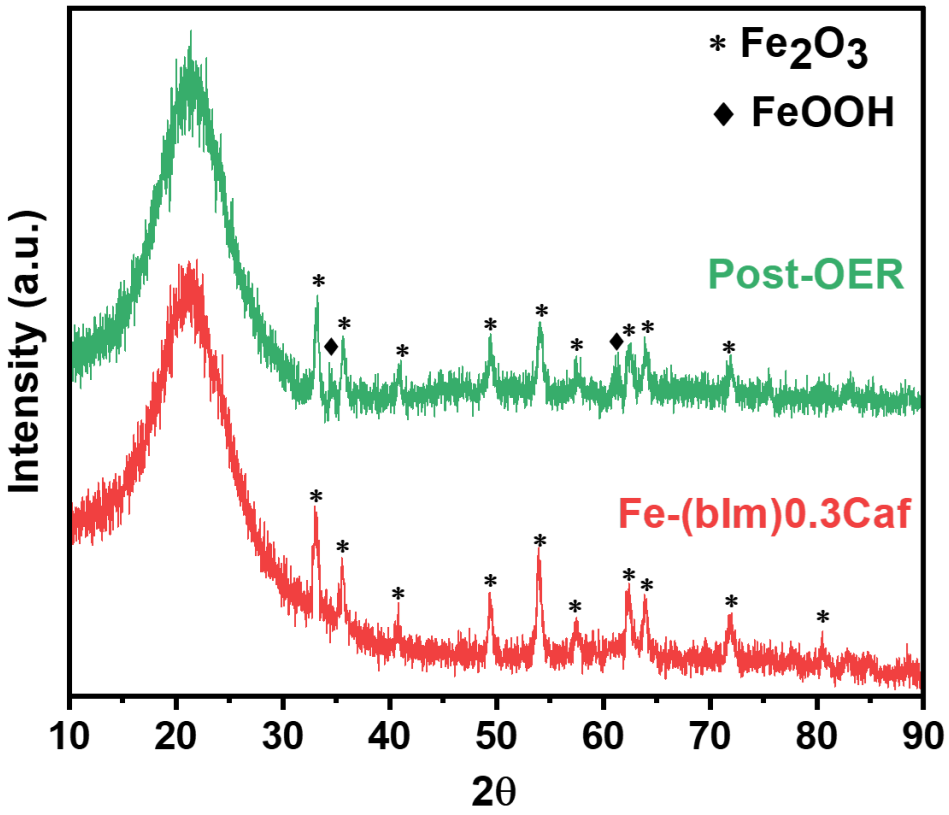

Figure 24. XRD pattern of Fe-(bIm)0.3Caf before and after the stability test

Furthermore, the XPS profiles of the sample was analyzed after the durability test (**Figure 25**), yielding results consistent with those of the CP and morphology analyses. The Fe 2p, C 1s, and O 1s spectra exhibited all deconvolution peak patterns similar to those of the initial sample spectra. Particularly, the Fe 2p spectrum (**Figure 25a**) demonstrated that after stability testing, the ratio of Fe^{3+} and Fe^{2+} ions were higher, with a value of 0.94, than the initial ratio of 0.70. This increase in ratio is attributed to the oxidation process, leading to the formation of FeOOH. Additionally, the C 1s and O 1s spectra (**Figure 25b and c**) exhibited a negative shift in binding energy after the stability test. After the 30 h stability test, Fe-(bIm)0.3Caf exhibited all deconvolutionpeaks fractions distribution similar to that of its initial state. The maintenance of OER activity resulted from the positive correlation between the O−C=O groups and the OER activity, determined based on the atomic ratio between O−C=O and C−O−C. This ratio increased from an initial value of 0.87 to 0.89 after the test, exhibiting approximately equivalent values before and after the test, which explains the substantially high activity retention of Fe-(bIm)0.3Caf after the durability test.

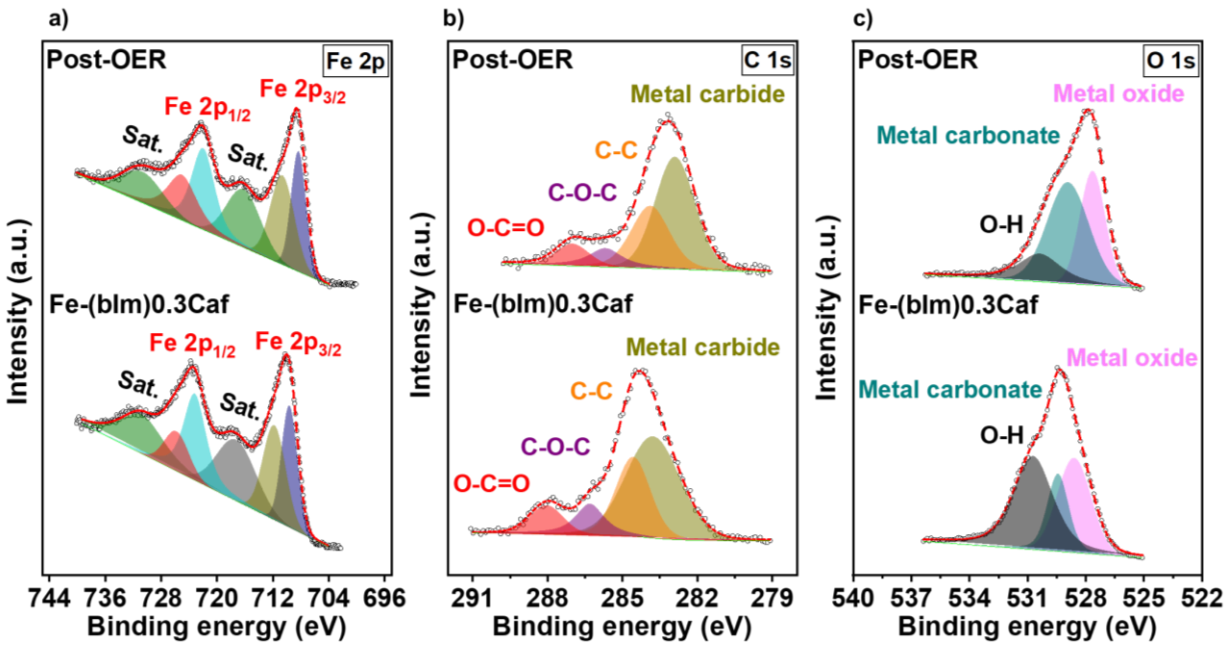

Figure 25. High-resolution XPS spectra of a) Fe 2p b) C 1s c) O 1s from Fe-(bIm)0.3Caf initial and after stability test

4.4 Conclusion

In summary, hematite nanocrystals, with spherical and rhombohedral morphologies, were interface functionalized under ligand supports to successfully synthesize catalyst nanoparticles using a simple one-pot hydrothermal pathway. Specifically, among the analyzed samples, the mixed-ligand sample, Fe-(bIm)0.3Caf, exhibited superior activity owing to the effects of oxygen vacancies on the adsorption of intermediates on the catalyst surface and modification of the electronic structure. Owing to the MSIs effects, the OER mechanism tends to shift from the AEM to LOM, improving the activity. Furthermore, the effects of MSIs result in the stabilization of metal compounds and enhancement of the covalent characteristics of the M–O bond, maintaining a balance between the AEM and LOM to ensure the stability and efficiency of catalysts. Moreover, the introduction of electron-withdrawing (–COOH) and electron-donating ($–NH_2$) groups into all synthesized samples enhances the OER activity , especially in the case of mixed-ligand Fe-(bIm)0.3Caf compared to commercial Fe_2O_3. Additionally, strong interactions between the metal species and carbon matrix can prevent aggregation of hematite nanocrystals, maintaining the durability of electrocatalysts. Furthermore, the higher electronegativity of the heteroatoms N and O in various functional groups results in stronger MSIs, which combined with oxygen vacancies, mitigate the issue of the low conductivity of Fe_2O_3. These effects collectively contribute to the application potential of Fe-(bIm)0.3Caf as an electrocatalyst possessing a high OER activity, facilitating a low overpotential of 264 mV at 10 mA cm^{-2} and small Tafel slope of 30 mV dec^{-1}. This study demonstrates the importance of the surface engineering and interface functionalization of hematite nanocrystals in enhancing the OER activity. In conclusion, this study introduces a new simple pathway for synthesizing interface-functionalized hematite nanocrystals, focusing on mixed ligands, which can be used to fabricate electrocatalysts with efficient and durable OER performances under alkaline conditions.

5. Recommendation for future work

Mixed ligands facilitate interface-functionalized hematite nanocrystals exhibit great potential in OER when

owning activity and stability with good performance. Besides, with simple preparation methodology is one-pot hydrothermal using low temperature, interface-functionalized hematite using Iron nitrate and 2 ligands benzimidazole and caffeine with easy-found and low cost as main components, which suitable for using in industry. However, electrochemical activity can be improved for better performance.

For intensive research, there are some directions for enhancing exhibition at lowing overpotential and long-term durability such as

- Combine two metal components with secondary metal such as Nickel, Cobalt,…
- Combine another ligands

References

[1] Global Carbon Project. (December 5, 2023). Annual carbon dioxide (CO_2) emissions worldwide from 1940 to 2023 (in billion metric tons) [Graph]. In *Statista*. Retrieved May 17, 2024, from https://www.statista.com/statistics/276629/global-co2-emissions/

[2] Cai Z, Xiuming B, Wang P, Ho J, Yang J, Wang X. Recent Advances on Layered Double Hydroxide Electrocatalysts for Oxygen Evolution Reaction. Journal of Materials Chemistry A. 2019;7.

[3] Over H. Fundamental Studies of Planar Single-Crystalline Oxide Model Electrodes (RuO_2, IrO_2) for Acidic Water Splitting. ACS Catalysis. 2021;11:8848-71.

[4] Yu Z-Y, Duan Y, Feng X-Y, Yu X, Gao M-R, Yu S-H. Clean and Affordable Hydrogen Fuel from Alkaline Water Splitting: Past, Recent Progress, and Future Prospects. Advanced Materials. 2021;33:2007100.

[5] Zhang J, Zhang Q, Feng X. Support and Interface Effects in Water-Splitting Electrocatalysts. Advanced Materials. 2019;31:1808167.

[6] Chen S, Huang H, Jiang P, Yang K, Diao J, Gong S, et al. Mn-Doped RuO2 Nanocrystals as Highly Active Electrocatalysts for Enhanced Oxygen Evolution in Acidic Media. ACS Catalysis. 2020;10:1152-60.

[7] Yang X, Li Y, Deng L, Li W, Ren Z, Yang M, et al. Synthesis and characterization of an IrO 2 –Fe 2 O 3 electrocatalyst for the hydrogen evolution reaction in acidic water electrolysis. RSC Adv. 2017;7:20252-8.

[8] Zhang K, Zou R. Advanced Transition Metal-Based OER Electrocatalysts: Current Status, Opportunities, and Challenges. Small. 2021;17:2100129.

[9] Hao Y, Cao X, Lei C, Chen Z, Yang X, Gong M. Chemical oxygen species on electrocatalytic materials during oxygen evolution reaction. Materials Today Catalysis. 2023;2:100012.

[10] Suen N-T, Hung S-F, Quan Q, Zhang N, Xu Y-J, Chen HM. Electrocatalysis for the oxygen evolution reaction: recent development and future perspectives. Chemical Society Reviews. 2017;46:337-65.

[11] Rajput A, Kundu A, Chakraborty B. Recent Progress on Copper-Based Electrode Materials for Overall Water-Splitting. ChemElectroChem. 2021;8:1698-722.

[12] Li X-P, Huang C, Han W-K, Ouyang T, Liu Z-Q. Transition metal-based electrocatalysts for overall water splitting. Chinese Chemical Letters. 2021;32:2597-616.

[13] Wang J, Yue X, Yang Y, Sirisomboonchai S, Wang P, Ma X, et al. Earth-abundant transition-metal-based bifunctional catalysts for overall electrochemical water splitting: A review. Journal of Alloys and Compounds. 2020;819:153346.

[14] Haschke S, Pankin D, Petrov Y, Bochmann S, Manshina A, Bachmann J. Design Rules for Oxygen Evolution Catalysis at Porous Iron Oxide Electrodes: A 1000-Fold Current Density Increase. ChemSusChem. 2017;10:3644-51.

[15] Mugheri AQ, Tahira A, Aftab U, Abro MI, Chaudhry SR, Amaral L, et al. Facile efficient earth abundant NiO/C composite electrocatalyst for the oxygen evolution reaction. RSC Advances. 2019;9:5701-10.

[16] Wang X, Shi G. An introduction to the chemistry of graphene. Physical Chemistry Chemical Physics. 2015;17:28484-504.

[17] Jiang X, Zhang W, Xu G-R, Lai J, Wang L. Interface engineering of metal nanomaterials enhance the electrocatalytic water splitting and fuel cell performance. Electrochemical Science Advances. 2022;2:e2100066.

[18] Zhu K, Shi F, Zhu X, Yang W. The roles of oxygen vacancies in electrocatalytic oxygen evolution reaction. Nano Energy. 2020;73:104761.

[19] Zhang X, Liu Y, Ma X, Liu X, Zhang R, Wang Y. Metal–Support Interaction of Carbon–Based Electrocatalysts for Oxygen Evolution Reaction. Nanoenergy Advances. 2023;3:48-72.

[20] Peng M, Huang J, Zhu Y, Zhou H, Hu Z, Liao Y-K, et al. Structural Anisotropy Determining the Oxygen Evolution Mechanism of Strongly Correlated Perovskite Nickelate Electrocatalyst. ACS Sustainable Chemistry & Engineering. 2021;9:4262-70.

[21] Zhang Y, Yu Z, Jiang R, Huang J, Hou Y, Yang F, et al. A novel ligand with –NH2 and –COOH-decorated Co/Fe-based oxide for an efficient overall water splitting: dual modulation roles of active sites and local electronic structure. Catalysis Science & Technology. 2020;10:6266-73.

[22] Zhang Y, Yang J, Yu Z, Hou Y, Jiang R, Huang J, et al. Modulating carbon-supported transition metal oxide by electron-giving and electron-absorbing functional groups towards efficient overall water splitting. Chemical Engineering Journal. 2021;416:129124.

[23] Zhang L, Chen Y, Liu G, Li Z, Liu S, Tiwari SK, et al. Construction of CoP/Co2P Coexisting Bifunctional Self-Supporting Electrocatalysts for High-Efficiency Oxygen Evolution and Hydrogen Evolution. ACS Omega. 2022;7:12846-55.

[24] Arakha M, Pal S, Samantarrai D, Panigrahi TK, Mallick BC, Pramanik K, et al. Antimicrobial activity of iron oxide nanoparticle upon modulation of nanoparticle-bacteria interface. Scientific Reports. 2015;5:14813.

[25] Narayanan KB, Han SS. One-Pot Green Synthesis of Hematite (α-Fe2O3) Nanoparticles by Ultrasonic Irradiation and Their In Vitro Cytotoxicity on Human Keratinocytes CRL-2310. Journal of Cluster Science. 2016;27:1763-75.

[26] Kandori K, Tamura S, Ishikawa T. Inner structure and properties of diamond-shaped and spherical α-Fe2O3 particles. Colloid and Polymer Science. 1994;272:812-9.

[27] Tadic M, Kopanja L, Panjan M, Lazovic J, Tadic BV, Stanojevic B, et al. Rhombohedron and plate-like hematite (α-Fe2O3) nanoparticles: synthesis, structure, morphology, magnetic properties and potential biomedical applications for MRI. Materials Research Bulletin. 2021;133:111055.

[28] Rodriguez RD, Demaille D, Lacaze E, Jupille J, Chaneac C, Jolivet J-P. Rhombohedral Shape of Hematite Nanocrystals Synthesized via Thermolysis of an Additive-free Ferric Chloride Solution. The Journal of Physical Chemistry C. 2007;111:16866-70.

[29] Wang Y, Xue S, Lin Q, Song D, He Y, Liu L, et al. Particle-based hematite crystallization is invariant to initial particle morphology. Proceedings of the National Academy of Sciences. 2022;119:e2112679119.

[30] Li Z, Pan Z, Wang Y. Enhanced adsorption of cationic Pb(II) and anionic Cr(VI) ions in aqueous solution by amino-modified nano-sized illite-smectite clay. Environmental Science and Pollution Research. 2019;26:11126-39.

[31] Fang Y, Zhang L, Zhao Q, Wang X, Jia X. Highly Selective Visible-Light Photocatalytic Benzene Hydroxylation to Phenol Using a New Heterogeneous Photocatalyst UiO-66-NH2-SA-V. Catalysis Letters. 2019;149:2408-14.

[32] Liu J, Bai H, Wang Y, Liu Z, Zhang X, Sun DD. Self-Assembling TiO2 Nanorods on Large Graphene Oxide Sheets at a Two-Phase Interface and Their Anti-Recombination in Photocatalytic Applications. Advanced Functional Materials. 2010;20:4175-81.

[33] Zhao JG, Zhang HH. Hydrothermal synthesis and characterization of ZnS hierarchical microspheres. Superlattices and Microstructures. 2012;51:663-7.

[34] Sobhanardakani S, Jafari A, Zandipak R, Meidanchi A. Removal of heavy metal (Hg(II) and Cr(VI)) ions from aqueous solutions using Fe2O3@SiO2 thin films as a novel adsorbent. Process Safety and Environmental Protection. 2018;120:348-57.

[35] Chamritski I, Burns G. Infrared- and Raman-Active Phonons of Magnetite, Maghemite, and Hematite: A Computer Simulation and Spectroscopic Study. The Journal of Physical Chemistry B. 2005;109:4965-8.

[36] Bersani D, Lottici PP, Montenero A. Micro-Raman investigation of iron oxide films and powders produced by sol–gel syntheses. Journal of Raman Spectroscopy. 1999;30:355-60.

[37] Jubb AM, Allen HC. Vibrational Spectroscopic Characterization of Hematite, Maghemite, and Magnetite Thin Films Produced by Vapor Deposition. ACS Applied Materials & Interfaces. 2010;2:2804-12.

[38] Lübbe M, Gigler AM, Stark RW, Moritz W. Identification of iron oxide phases in thin films grown on Al2O3(0 0 0 1) by Raman spectroscopy and X-ray diffraction. Surface Science. 2010;604:679-85.

[39] Jiang L, You T, Yin P, Shang Y, Zhang D, Guo L, et al. Surface-enhanced Raman scattering spectra of adsorbates on Cu2O nanospheres: charge-transfer and electromagnetic enhancement. Nanoscale.

2013;5:2784-9.

[40] Xiao Y, Wang Y, Xiao M, Liu C, Hou S, Ge J, et al. Regulating the pore structure and oxygen vacancies of cobaltosic oxide hollow dodecahedra for an enhanced oxygen evolution reaction. NPG Asia Materials. 2020;12:73.

[41] Yang Y, Zhou Q, Yang J, Qian D, Xiong Y, Li Z, et al. Metal–organic framework derived CoS2/FeS-MOF with abundant heterogeneous interface as bifunctional electrocatalyst for electrolysis of water. International Journal of Hydrogen Energy. 2022;47:33728-40.

[42] Kwon J, Han H, Jo S, Choi S, Chung KY, Ali G, et al. Amorphous Nickel–Iron Borophosphate for a Robust and Efficient Oxygen Evolution Reaction. Advanced Energy Materials. 2021;11:2100624.

[43] Zhu J, Wang P, Zhang X, Zhang G, Li R, Li W, et al. Dynamic structural evolution of iron catalysts involving competitive oxidation and carburization during CO2 hydrogenation. Science Advances.8:eabm3629.

[44] Li D, Baydoun H, Kulikowski B, Brock SL. Correction to Boosting Catalytic Performance of Iron Phosphide Nanorods for the Oxygen Evolution Reaction by Incorporation of Manganese. Chemistry of Materials. 2017;29:7630-.

[45] Roy A, Mukhopadhyay AK, Das SC, Bhattacharjee G, Majumdar A, Hippler R. Surface Stoichiometry and Optical Properties of Cux–TiyCz Thin Films Deposited by Magnetron Sputtering. Coatings2019.

[46] Maknakorn W, Jutaporn P, Khongnakorn W. Coagulation and adsorption as pretreatments of thin film composite-forward osmosis (TFC-FO) for ink printing wastewater treatment. Water Science and Technology. 2019;79.

[47] Ejsmont A, Kadela K, Grzybek G, Darvishzad T, Słowik G, Lofek M, et al. Speciation of Oxygen Functional Groups on the Carbon Support Controls the Electrocatalytic Activity of Cobalt Oxide Nanoparticles in the Oxygen Evolution Reaction. ACS Applied Materials & Interfaces. 2023;15:5148-60.

[48] Yang BS, Oh S, Kim YJ, Han SJ, Lee HW, Kim H, et al. The Anomalous Effect of Oxygen Ratio on the Mobility and Photobias Stability of Sputtered Zinc–Tin–Oxide Transistors. IEEE Transactions on

Electron Devices. 2014;61:2071-7.

[49] Hou F, Gorthy R, Mardon I, Tang D, Goode C. Low voltage environmentally friendly plasma electrolytic oxidation process for titanium alloys. Scientific Reports. 2022;12:6037.

[50] Li Y, Tan B, Wu Y. Mesoporous Co3O4 nanowire arrays for lithium ion batteries with high capacity and rate capability. Nano letters. 2008;8 1:265-70.

[51] Xu L, Jiang Q, Xiao Z, Li X, Huo J, Wang S, et al. Plasma-Engraved Co3O4 Nanosheets with Oxygen Vacancies and High Surface Area for the Oxygen Evolution Reaction. Angewandte Chemie International Edition. 2016;55:5277-81.

[52] Dong W, Zhou H, Mao B, Zhang Z, Liu Y, Liu Y, et al. Efficient MOF- derived V–Ni3S2 nanosheet arrays for electrocatalytic overall water splitting in alkali. International Journal of Hydrogen Energy. 2021;46:10773-82.

[53] Palem RR, Meena A, Soni R, Meena J, Lee S-H, Patil SA, et al. Fabrication of Fe2O3 nanostructure on CNT for oxygen evolution reaction. Ceramics International. 2022;48:29081-6.

[54] Samanta A, Jana S. Ni-, Co-, and Mn-Doped Fe2O3 Nano-Parallelepipeds for Oxygen Evolution. ACS Applied Nano Materials. 2021;4:5131-40.

[55] Luo W, Wang J, Hu J, Ji Y, Streb C, Song Y-F. Composite Metal Oxide-Carbon Nanotube Electrocatalysts for the Oxygen Evolution and Oxygen Reduction Reactions. ChemElectroChem. 2018;5.

[56] Yang Z, Tan H, Qi Y, Ma S, Bai J, Liu L, et al. Preparation and characterization of nanostructured Fe-doped CoTe2 electrocatalysts for the oxygen evolution reaction. Dalton Transactions. 2023;52.

[57] Liu Q, Zhao H, Jiang M, Kang Q, Zhou W, Wang P, et al. Boron Enhances Oxygen Evolution Reaction Activity over Ni Foam-Supported Iron Boride Nanowires. Journal of Materials Chemistry A. 2020;8.

[58] Sagar P, Yogesh K, Syed A, Marraiki N, Elgorban AM, Zaghloul NSS, et al. Studies on the effect of crystalline Fe2O3 on OER performance of amorphous NiOOH electrodeposited on stainless steel substrate. Chemical Papers. 2022;76:7195-203.

[59] Kim J, Heo JN, Do JY, Chava RK, Kang M. Electrochemical Synergies of Heterostructured Fe2O3-

MnO Catalyst for Oxygen Evolution Reaction in Alkaline Water Splitting. Nanomaterials2019.

[60] Alduhaish O, Ubaidullah M, Al-Enizi AM, Alhokbany N, Alshehri SM, Ahmed J. Facile Synthesis of Mesoporous α-Fe2O3@g-C3N4-NCs for Efficient Bifunctional Electro-catalytic Activity (OER/ORR). Scientific Reports. 2019;9:14139.

[61] Ali A, Liang F, Feng H, Tang M, Jalil Shah S, Ahmad F, et al. Gram-scale production of in-situ generated iron carbide nanoparticles encapsulated via nitrogen and phosphorous co-doped bamboo-like carbon nanotubes for oxygen evolution reaction. Materials Science for Energy Technologies. 2023;6:301-9.

[62] Srinivasan S, Rathinam Y, Ganesan R, Alagarsamy A. Construction of Fe2O3 Nanoparticles Decorated for a Highly Efficient Oxygen Evolution Reaction Activity. Energy & Fuels. 2023;37:15976-85.

[63] Jiang W, Lehnert W, Shviro M. The Influence of Loadings and Substrates on the Performance of Nickel-Based Catalysts for the Oxygen Evolution Reaction. ChemElectroChem. 2023;10:e202200991.

[64] Ansari MS, Kim H. Enhanced electrocatalytic oxygen evolution reaction kinetics using dual-phase engineering of self-supported hierarchical NiCoV(OH)x nanowire arrays. Fuel. 2021;304:121309.

[65] Kauffman DR, Deng X, Sorescu DC, Nguyen-Phan T-D, Wang C, Marin CM, et al. Edge-Enhanced Oxygen Evolution Reactivity at Ultrathin, Au-Supported Fe2O3 Electrocatalysts. ACS Catalysis. 2019;9:5375-82.

[66] Ge K, Sun S, Zhao Y, Yang K, Wang S, Zhang Z, et al. Facile Synthesis of Two-Dimensional Iron/Cobalt Metal–Organic Framework for Efficient Oxygen Evolution Electrocatalysis. Angewandte Chemie International Edition. 2021;60:12097-102.

[67] Yan L, Bing J, Wu H. The behavior of ozone on different iron oxides surface sites in water. Scientific Reports. 2019;9.